

# Journal of Geophysical Research: Solid Earth

## RESEARCH ARTICLE

10.1002/2014JB011492

**Key Points:**

- A new 3-D viscoelastic interseismic deformation model
- The slip deficit rate distribution is jointly inverted with GPS and InSAR data
- Seven potential asperities on the XAZ fault system

**Correspondence to:**X. Xu,  
xiweixu@vip.sina.com**Citation:**

Jiang, G., X. Xu, G. Chen, Y. Liu, Y. Fukahata, H. Wang, G. Yu, X. Tan, and C. Xu (2015), Geodetic imaging of potential seismogenic asperities on the Xianshuihe-Anninghe-Zemuhe fault system, southwest China, with a new 3-D viscoelastic interseismic coupling model, *J. Geophys. Res. Solid Earth*, 120, 1855–1873, doi:10.1002/2014JB011492.

Received 29 JUL 2014

Accepted 28 JAN 2015

Accepted article online 3 FEB 2015

Published online 16 MAR 2015

## Geodetic imaging of potential seismogenic asperities on the Xianshuihe-Anninghe-Zemuhe fault system, southwest China, with a new 3-D viscoelastic interseismic coupling model

Guoyan Jiang<sup>1</sup>, Xiwei Xu<sup>1</sup>, Guihua Chen<sup>1</sup>, Yajing Liu<sup>2</sup>, Yukitoshi Fukahata<sup>3</sup>, Hua Wang<sup>4</sup>, Guihua Yu<sup>1</sup>, Xibin Tan<sup>1</sup>, and Caijun Xu<sup>5</sup>

<sup>1</sup>Key Laboratory of Active Tectonics and Volcano, Institute of Geology, China Earthquake Administration, Beijing, China,

<sup>2</sup>Department of Earth and Planetary Sciences, McGill University, Montréal, Quebec, Canada, <sup>3</sup>Disaster Prevention Research Institute, Kyoto University, Kyoto, Japan, <sup>4</sup>Department of Surveying Engineering, Guangdong University of Technology, Guangzhou, China, <sup>5</sup>School of Geodesy and Geomatics, Wuhan University, Wuhan, China

**Abstract** We use GPS and interferometric synthetic aperture radar (InSAR) measurements to image the spatial variation of interseismic coupling on the Xianshuihe-Anninghe-Zemuhe (XAZ) fault system. A new 3-D viscoelastic interseismic deformation model is developed to infer the rotation and strain rates of blocks, postseismic viscoelastic relaxation, and interseismic slip deficit on the fault surface discretized with triangular dislocation patches. The inversions of synthetic data show that the optimal weight ratio and smoothing factor are both 1. The successive joint inversions of geodetic data with different viscosities reveal six potential fully coupled asperities on the XAZ fault system. Among them, the potential asperity between Shimian and Mianning, which does not exist in the case of  $10^{19}$  Pa s, is confirmed by the published microearthquake depth profile. Besides, there is another potential partially coupled asperity between Daofu and Kangding with a length scale up to 140 km. All these asperity sizes are larger than the minimum resolvable wavelength. The minimum and maximum slip deficit rates near the Moxi town are 7.0 and 12.7 mm/yr, respectively. Different viscosities have little influence on the roughness of the slip deficit rate distribution and the fitting residuals, which probably suggests that our observations cannot provide a good constraint on the viscosity of the middle lower crust. The calculation of seismic moment accumulation on each segment indicates that the Songlinkou-Selaha (S4), Shimian-Mianning (S7), and Mianning-Xichang (S8) segments are very close to the rupture of characteristic earthquakes. However, the confidence level is confined by sparse near-fault observations.

### 1. Introduction

Time-dependent seismic hazard is associated with contemporary stress state of active faults and its variation in time [e.g., Heidbach and Ben-Avraham, 2007]. Stress loading on a fault is mainly from two aspects: (1) long-term tectonic motion of plates and (2) irregular coseismic and postseismic stress perturbations from nearby earthquakes. The tectonic stress loading is directly linked to interseismic slip deficit on the fault, also named as “back slip.” In the past several decades, a number of 2-D and 3-D elastic-viscoelastic interseismic deformation models were developed to invert slip deficit rates using geodetic observations [e.g., Fukahata et al., 2004; Johnson and Fukuda, 2010; Johnson and Segall, 2004; Matsu'ura et al., 1986; Meade and Loveless, 2009; McCaffrey, 2005; Nur and Mavko, 1974; Savage and Burford, 1970, 1973; Savage and Prescott, 1978]. The 3-D viscoelastic interseismic deformation models have both numerical and analytical styles. The numerical models are usually built with finite elements for the seismogenic zone of subduction thrust faults [e.g., Hyodo and Hirahara, 2003; Wang et al., 2001, 2012]. The interseismic crustal displacements are taken as the superposition of steady state plate convergence and fully coupled zone on the subduction fault, which can be equivalently described as backward slip at the convergence rate.

Table 1 lists the features of three classical 3-D analytical viscoelastic models. Matsu'ura and Sato [1989] presented a 3-D viscoelastic model for convergent plate boundaries. The ground deformation in an earthquake cycle was decomposed into the steady slip deficit on the seismogenic zone, the viscoelastic effect of steady slip on the interface above the lithosphere-asthenosphere boundary, and the periodic seismic slip. The Green's function was calculated by using the dislocation model in half-space of a viscoelastic substratum underlain in

**Table 1.** The Features of Published 3-D Analytical Viscoelastic Interseismic Deformation Models

Feature	<i>Matsu'ura and Sato</i> [1989]	<i>Pollitz et al.</i> [2008]	<i>Johnson and Fukuda</i> [2010]	Our Model
Block motion	✓	✓	✓	✓
Intrablock strain	✗	✓	✗	✓
Fault coupling ratio	✗	✗	✓	✓
Fault-normal slip discontinuity	✓	✗	✓	✓
Strike variation	✗	✓	✓	✓
Fault surface discretization	✗	✓	✓	✓
RDE/TDE	RDE	RDE	RDE	TDE
Lateral heterogeneity	✗	✓	✗	✗
Distributed dislocation sources	✗	✓	✗	✗

an elastic superstratum. In the model by *Pollitz et al.* [2008], the large-scale interseismic velocities were attributed to (1) viscoelastic relaxation from major earthquakes and interseismic moment release on the plate boundary faults, (2) distributed fault dislocations in the plate interior, (3) lateral heterogeneity in the elastic lithosphere, as well as (4) block rotation and intrablock strain. *Johnson and Fukuda* [2010] developed another 3-D viscoelastic model for intraplate interseismic deformation, where the patches on the fault interface were supposed to be either fully coupled or creeping under constant shear stress during the interseismic period. The crustal deformation was assumed to be a sum of the steady long-term fault slip (block motion), the strain accumulation due to the back slip to cancel long-term slip discontinuities above the locked depth, and the viscoelastic relaxation effect of past earthquakes. In particular, the fault-normal slip discontinuity on dipping faults was considered in their model. Building upon the model by *Johnson and Fukuda* [2010], we introduce triangular dislocation elements (TDEs) to construct the fault surface. Compared with rectangular dislocation elements (RDEs), the application of TDEs allows a sophisticated fault geometric model to be established without dislocation overlaps and gaps, which may negatively influence the resulting slip models and can induce stress singularity at their edges [*Jiang et al.*, 2013]. Besides, we explain the interseismic velocities including the contribution from nonrecoverable homogeneous intrablock strain.

Due to the spatial and temporal limitation in geodetic instrumentation coverage, at early times, researchers could only obtain a single slip rate for each fault segment [e.g., *Johnson and Segall*, 2004; *Savage and Lisowski*, 1998]. In recent years, the improvements in space-based geodetic technologies (GPS and interferometric synthetic aperture radar (InSAR)) with growing coverage and accuracy provide us an opportunity to image more subtle features of interseismic fault creeping and coupling. Not only the locked asperities on the intraplate faults [e.g., *Evans et al.*, 2012; *Schmidt et al.*, 2005] and subduction zones [e.g., *Bürgmann et al.*, 2005; *Kanda et al.*, 2013; *Noda and Lapusta*, 2013] can be identified with greater details than before, episodic slow events below the seismogenic zone have also been discovered in many subduction zones [e.g., *Dragert et al.*, 2001; *McCaffrey et al.*, 2008; *Ohta et al.*, 2006; *Liu*, 2014]. Geodetic instrumentation near major fault zones is starting to reveal a full spectrum of fault deformation modes from steady loading to dynamic rupture.

The Xianshuihe-Anninghe-Zemuhe (XAZ) fault system, consisting of the Xianshuihe fault, Anninghe fault, and Zemuhe fault, is located in the junction zone of the Sichuan-Yunnan terrace, Songpan-Ganzi fold, and south China block (Figure 1), which is a region of intensive tectonic activities in the Tibetan Plateau. There have been 19 earthquakes of  $M \geq 6.5$  on this fault system since 1700 [*Wen et al.*, 2008a]. The sinistral strike-slip Xianshuihe fault has prominent seismic activities and plays a significant role in accommodating the postcollisional convergence between the Eurasian and Indian plates [e.g., *Deng et al.*, 1979; *Tapponier and Molnar*, 1977]. Over the past several decades, many researchers have analyzed the seismic hazards of the XAZ fault system. The average earthquake recurrence intervals of the XAZ fault system from paleoseismologic records indicate that the fault segment between Bamei and Kangding on the Xianshuihe fault and the Anninghe fault is probably close to rupture [e.g., *Ran et al.*, 2008; *Wen et al.*, 2008a; *Zhou et al.*, 2001a]. This estimate is similar to the seismic gaps identified by the *b* value distributions from modern seismic records [e.g., *Wen et al.*, 2008b; *Yi et al.*, 2008]. Additionally, tectonic stressing rates of primary strike-slip faults in the Tibetan Plateau from GPS observations show the highest value on the Xianshuihe fault up to  $\sim 7.05$  kPa/yr [*Jiang et al.*, 2014]. All these published studies indicate that the XAZ fault system may be in a high risk of large earthquakes.

To provide another independent reference, we invert the interseismic slip deficit rate distribution on the XAZ fault system with GPS and InSAR observations in order to determine the locations and sizes of potentially

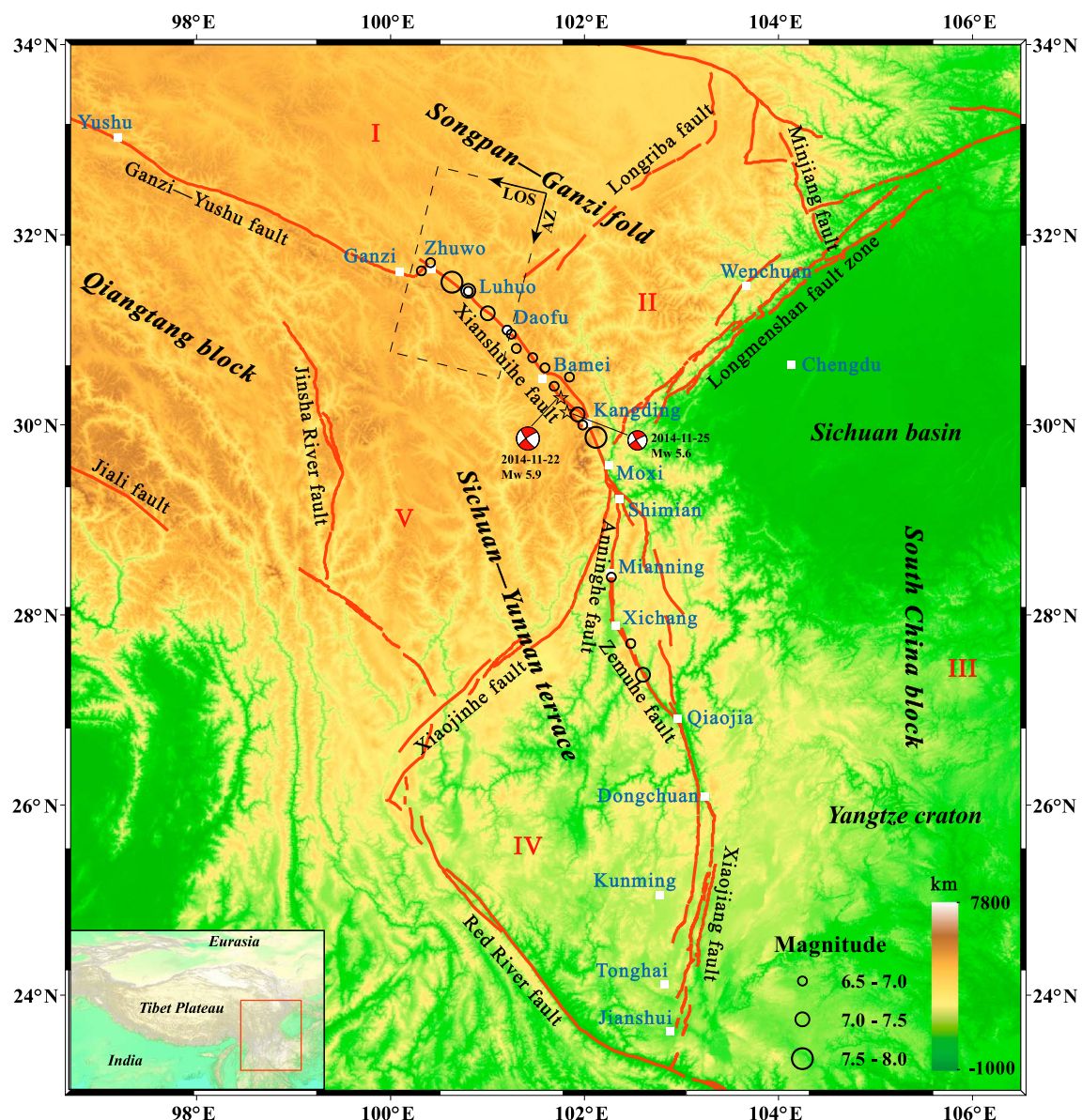


**Figure 1.** Tectonic and topographic map in the eastern Tibetan Plateau and its surrounding regions, as well as historical earthquakes (black circles) of  $M \geq 6.5$  since 1700 on the XAZ fault system. The two black stars represent the two events that struck the northwest of Kangding (<http://earthquake.usgs.gov/earthquakes>) in November 2014. The red lines denote the major boundary faults. The dashed rectangle outlines the coverage of InSAR data in Figure 3b. The two arrows on its upright corner show the radar line of sight (LOS) and azimuth directions, respectively. The study region is divided into five blocks: I, Ahba block; II, Longmenshan block; III, south China block; IV, the southern subblock of the Sichuan-Yunnan terrace; and V, the northern subblock of the Sichuan-Yunnan terrace.

locked asperities. TDEs are incorporated to build a finite and nonplanar fault geometric model. A new 3-D viscoelastic interseismic deformation model is constructed to quantify the rotation and strain rates of blocks, postseismic viscoelastic relaxation, and interseismic slip deficit. Finally, we explore the impact of middle lower crust rheology in western Sichuan on the inversion results and analyze the potential asperity distribution on the fault system with their implications for seismic hazards.

## 2. Regional Tectonic Setting

### 2.1. Block Division

In the tectonic junction zone of western Sichuan (Figure 1), where the XAZ fault system is located, the interactions among the Songpan-Ganzi fold, Sichuan-Yunnan terrace, and south China block caused noticeable tectonic

Elastic H=20 km $V_p = 6.05 \text{ km/s}$ , $V_s = 3.40 \text{ km/s}$ $\rho = 2.73 \text{ g/cm}^3$
Viscoelastic H=30 km $V_p = 5.85 \text{ km/s}$ , $V_s = 3.20 \text{ km/s}$ $\rho = 2.69 \text{ g/cm}^3$

**Figure 2.** The two-layered crustal model of the eastern Tibetan Plateau used in our calculation.

secondary blocks by the internal Xiaojinhe fault. The present-day eastward translation of the southern subblock is slower than that of the northern subblock [Shen et al., 2005]. The Xianshuihe fault is the eastern boundary of the northern subblock. The Anninghe and Zemuhe faults form the northeastern boundary of the southern subblock. The south China block, which includes the Sichuan basin and Yangtze craton, is considered to be a stable entirety on account of the absence of active faults and  $M > 7$  earthquakes [Deng et al., 2003]. The Anninghe and Zemuhe faults, associated with the segment from Moxi to Shimian of the Xianshuihe fault, are the northwestern boundary of the south China block. Therefore, we partition our research region into five blocks (Figure 1). The XAZ fault system is their sectional boundaries.

## 2.2. Crustal Structure

Many studies have investigated the crustal structure of the Sichuan basin and eastern Tibetan Plateau [e.g., Hu et al., 2011; Li et al., 2012; Liu et al., 2009; Sun et al., 2014; Wang et al., 2007, 2010, Y. Wang et al., 2013; Wang et al., 2014; Xu et al., 2013; Yang et al., 2012; Zhang et al., 2011; Xu and Song, 2010; Zhou et al., 2012]. The results from S and P wave receiver function analysis as well as ambient noise surface wave and P wave tomography show that the crustal thickness of the Ahba subblock ranges from 50 km to 60 km northwestward. The crustal thickness of the Longmenshan subblock is between 46 km and 55 km. The crustal thickness of the Sichuan basin is about 40~50 km. Two subblocks of the Sichuan-Yunnan terrace are 45~55 km and 55~65 km thick, respectively. According to these published results, we presume the average crustal thickness of the XAZ fault zone to be 55 km. The velocities of S and P wave in the shallow layer above the depth of ~20 km are about 3.4 km/s and 6.05 km/s, respectively.

In addition, there is a lower-velocity zone (LVZ) in the middle lower crust of the eastern Tibetan Plateau detected by seismic observations [e.g., Fu et al., 2010; Li et al., 2009; Wang et al., 2007, 2010, Y. Wang et al., 2013; Wang et al., 2014; Xu and Song, 2010; Yang et al., 2012; Yao et al., 2008; Zhang et al., 2011] as well as magnetotelluric data [Bai et al., 2010]. The LVZ probably indicates localized and limited partial melting crustal flow. The depth of LVZ ranges from 20 km to 50 km. The velocities of S and P wave in the LVZ are about 3.2 km/s and 5.85 km/s, respectively. For the LVZ rheology, Clark and Royden [2000] obtained a viscosity estimate of  $10^{18}$  Pa s within a fixed 15 km thick channel beneath the Sichuan-Yunnan terrace with low topographic gradient. Their subsequent model results also suggest a viscosity close to the earlier study [Clark et al., 2005; Royden et al., 2008]. However, Copley and McKenzie [2007] derived a different viscosity of  $\sim 10^{22}$  Pa s using models of fluid flow driven by horizontal pressure gradients from topography. Numerical experiments by Copley [2008] showed that surface motion modeled with different viscosities can resemble observed GPS velocities equally well. In this study, we start with the viscosity of  $10^{18}$  Pa s and then explore the influence on the inversion results by increasing viscosities.

Based on the aforementioned seismological and crustal flow studies, we stratify our model domain into a 20 km thick elastic upper crust followed by a 30 km thick LVZ in the middle lower crust, which is taken as a viscoelastic Maxwell body. The bottom 5 km thick lower crust is not included in our calculation. Figure 2 shows the crustal structure model of western Sichuan. On average, the crustal velocities of  $V_p$  and  $V_s$  in our research region are lower than the global continental crustal model [Wang et al., 2003; Yao et al., 2008]. The crustal densities are derived from a nonlinear empirical velocity-density formula [Brocher, 2005], which was first graphically presented by the Nafe-Drake curve [Ludwig et al., 1970].

deformation and many destructive earthquakes. The 2008  $M_w 7.9$  Wenchuan, 2010  $M_w 6.9$  Yushu, and 2013  $M_w 6.6$  Lushan earthquakes are dynamic manifestations of the tectonic activity. The Songpan-Ganzi fold is divided into the Ahba and Longmenshan subblocks by the newly identified Longriba fault [Xu et al., 2008]. These two subblocks have different present-day eastward translation velocities,  $\sim 11.4$  mm/yr (Ahba subblock) and  $\sim 8.5$  mm/yr (Longmenshan subblock), respectively. The northwestern part of the Xianshuihe fault about from Zhuwo to Daofu is the partial southwestern boundary of the Ahba subblock. The segment almost from Daofu to Moxi is the western boundary of the Longmenshan subblock. The southeastern Sichuan-Yunnan terrace is also divided into two

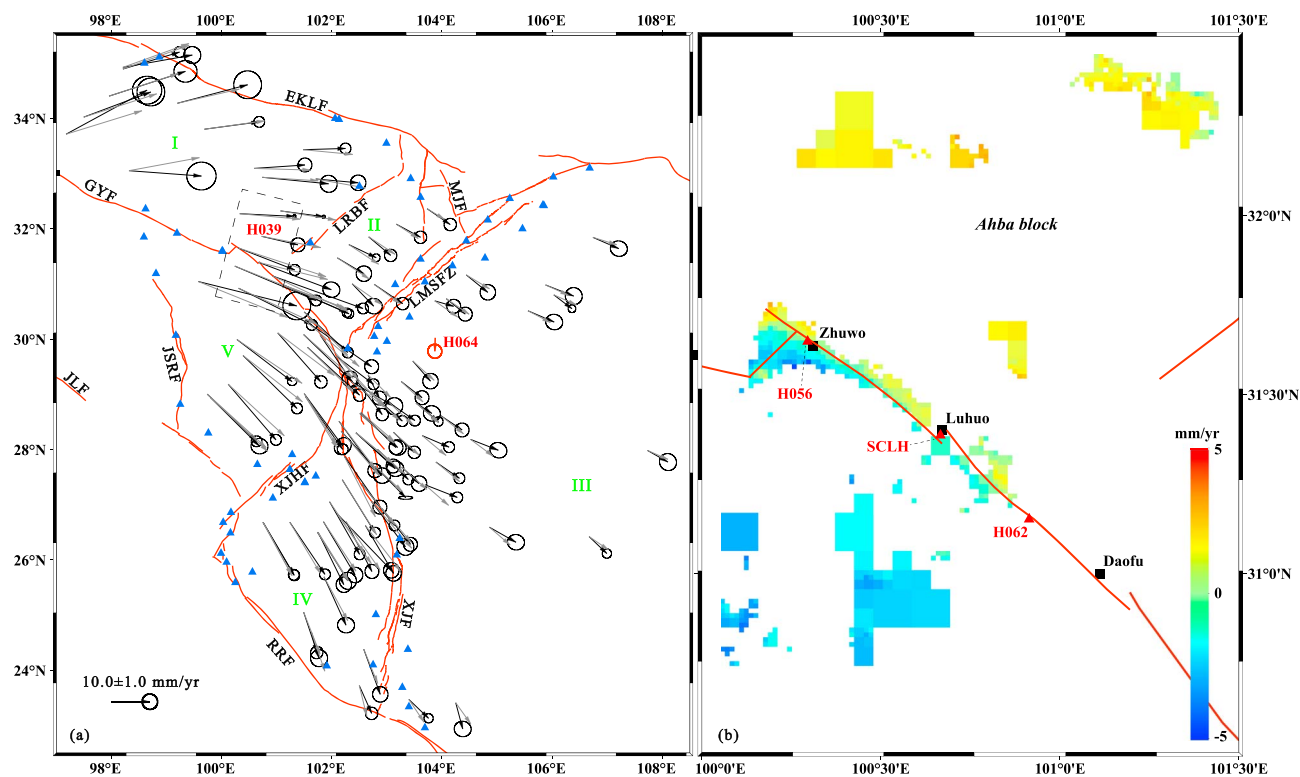


**Figure 3.** (a) Interseismic GPS velocities relative to the stable Eurasian plate and (b) downsampled InSAR LOS rate map. In Figure 3a, the black arrows with error ellipses of 95% confidence and gray arrows delineate the observed and predicted GPS velocities, respectively. The blue triangles mark the rejected GPS stations. The red arrow denotes an abnormal GPS velocity.

### 3. Geodetic Observations

#### 3.1. GPS Data

The GPS interseismic displacements relative to the stable Eurasia's reference frame used in our study are from 750 stations around the Tibetan Plateau obtained and reported by Liang *et al.* [2013]. Most measurements of these stations are over 10 years or have at least five campaigns. During this period, four great earthquakes (2001  $M_w$ 7.8 Kokoxili, 2008  $M_w$ 7.1 Yutian, 2008  $M_w$ 7.9 Wenchuan, and 2010  $M_w$ 6.9 Yushu) occurred in and around the Tibetan Plateau. The coseismic effect of these events as well as the postseismic displacements triggered by 2008 Wenchuan earthquake are removed from the GPS signals. Therefore, the plateau tectonic motion can be deemed as the only source of the GPS velocities. Among these measurements, we select 162 stations located in the Songpan-Ganzi fold, Sichuan-Yunnan terrace, and south China block for our analysis (Figure 3a).

However, not all the measurements from the selected GPS stations are suitable in our inversions. Two categories of stations should be excluded (Figure 3a). First, we excluded 61 stations within 40 km off the unmodeled faults such as the Ganzi-Yushu fault, eastern Kunlun fault, Longriba fault, Minjiang fault, Longmenshan fault zone, Xiaojinhe fault, Jinsha River fault, Red River fault, and Xiaojiang fault. The 40 km distance criterion is chosen to be about twice of the general locked depth of faults in the Tibetan Plateau. The ground displacements in this interval are greatly affected by interseismic fault coupling [Savage and Burford, 1973]. Second, we excluded data of the station H064, which has a velocity record different from nearby velocities by visual inspection. The measurements from the left 100 GPS stations are used in the following inversions.

#### 3.2. InSAR Data

InSAR images use repeated satellite surveys associated with the persistent scatterer interferometric radar analysis and multiinterferogram methods to detect the interseismic fault deformation signals. There have been successful applications around the world, such as the Hayward fault in the San Francisco Bay Area [Bürgmann *et al.*, 2006], the Altyn and Manyi faults in the Tibetan Plateau [Elliott *et al.*, 2008; Bell *et al.*, 2011],

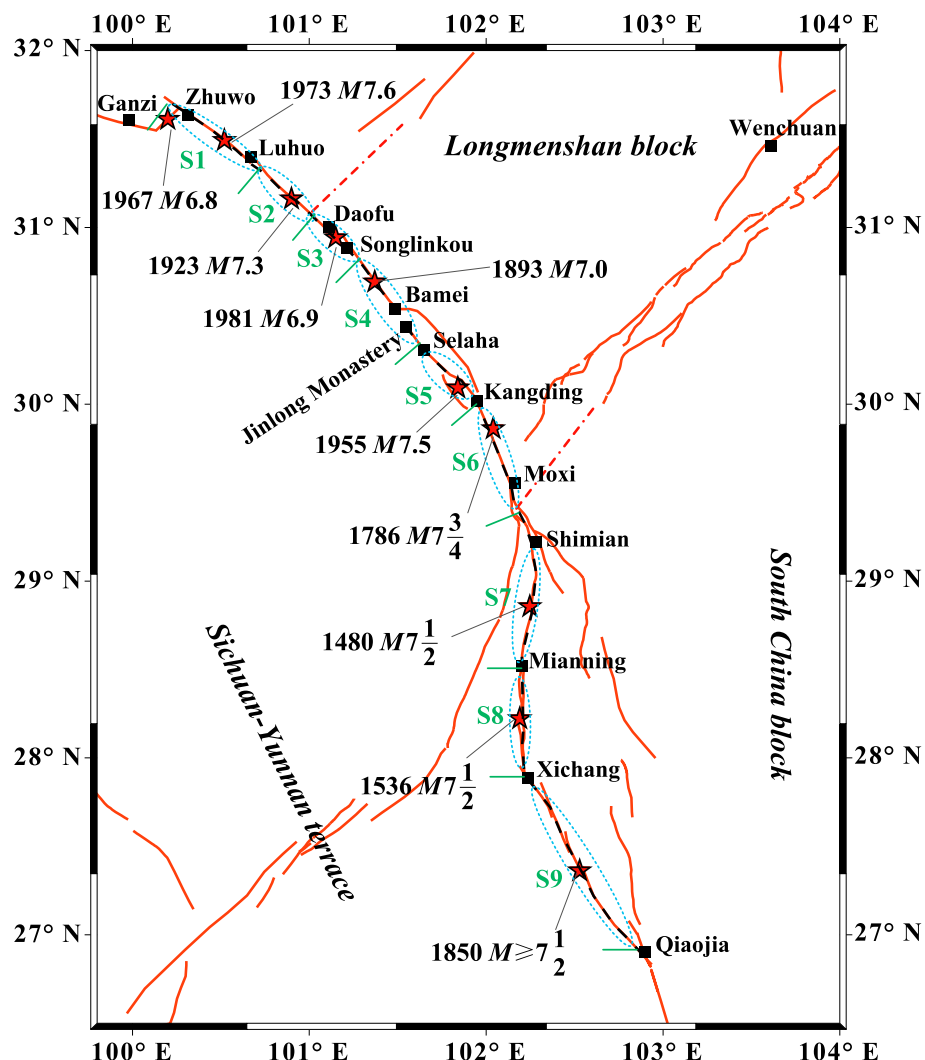


**Figure 4.** Earthquake rupture segment model of the XAZ fault system. The red stars denote the last earthquakes that occurred on 9 segments. The green dashed ellipses outline the rupture lengths of last earthquakes. The black dashed polyline is the modeled ground trace of the XAZ fault system.

the North Anatolian fault zone [Peyret *et al.*, 2013], and the North Chilean subduction zone [Béjar-Pizarro *et al.*, 2013]. The interseismic line of sight (LOS) deformation rate field used here is published by Wang *et al.* [2009], who also used a multiinterferogram method from a decade of SAR images acquired by the Envisat and ERS-1/2 satellites. The time span is from 6 January 1996 to 18 May 2008, which is coincident with the interval of GPS data since 1999. Although the last radar image was acquired after the 12 May 2008 Wenchuan earthquake, the overall coseismic influence in the InSAR coverage can be reduced by using the polynomial fitting during the orbital error correction, just like removing the large-scale deformation trend. Furthermore, the residual coseismic deformation can be reduced to a very low level after the deformation average of 12 years for the LOS rate map. The InSAR data mainly covers the segment approximately from Zhuwo to Luhuo of the Xianshuihe fault for ~90 km long and ~100 km wide on both sides.

To improve computational efficiency of our inversions and reduce the spatial correlation, we compressed the InSAR rate map with the quadtree sampling method [Jónsson *et al.*, 2002; Welstead, 1999]. The minimum and maximum sampling windows are set to be  $4 \times 4$  and  $32 \times 32$  pixels, respectively. The threshold root-mean-square value is 0.25 mm. Figure 3b shows the downsampled LOS rate field of 518 observations. Among them, 32 observations in the Ahba block and 15 observations in the northern subblock of the Sichuan-Yunnan terrace that are not consistent with the overall trend of deformation are excluded in our study. The numbers

**Table 2.** Characteristic Earthquake Parameters and Seismic Moment Accumulation of Nine Segments of the XAZ Fault System

Segment	Magnitude	Recurrence Interval (Year)	Reference	Annual $M_0$ Deficit (N m)	$M_0$ Accumulation Since Last Event (N m)	Equivalent Magnitude
S1	7.5	170	<i>Allen et al. [1991], Kato et al. [2007], and Ran and He [2006]</i>	$2.26 \times 10^{17}$	$9.25 \times 10^{18}$	$M_w 6.58$
S2	7.5	170	<i>Kato et al. [2007] and Ran and He [2006]</i>	$1.29 \times 10^{17}$	$1.17 \times 10^{17}$	$M_w 6.65$
S3	7.0	110	<i>Allen et al. [1991], Kato et al. [2007], and Ran and He [2006]</i>	$7.67 \times 10^{16}$	$2.53 \times 10^{18}$	$M_w 6.21$
S4	7.0	170	<i>Kato et al. [2007] and Ran and He [2006]</i>	$1.58 \times 10^{17}$	$1.89 \times 10^{19}$	$M_w 6.79$
S5	7.0	230	<i>Wen et al. [2008a]</i>	$1.21 \times 10^{17}$	$7.15 \times 10^{18}$	$M_w 6.51$
S6	$\geq 7.5$	340	<i>Allen et al. [1991], Kato et al. [2007], and Wen et al. [2008a]</i>	$1.16 \times 10^{17}$	$2.64 \times 10^{19}$	$M_w 6.89$
S7	7.5	700	<i>Qian et al. [1990], Ran et al. [2008], Wen [2000], Wen et al. [2008a], and Zhou et al. [2001b]</i>	$5.37 \times 10^{17}$	$2.87 \times 10^{20}$	$M_w 7.58$
S8	7.5	500	<i>Yi et al. [2004] and Wen et al. [2008a]</i>	$2.47 \times 10^{17}$	$1.18 \times 10^{20}$	$M_w 7.32$
S9	7.5	2000	<i>He and Ren [2003], Ren and Li [1989], H. Wang et al. [2013], Wen et al. [2008a], and Tian et al. [2008]</i>	$3.86 \times 10^{17}$	$6.33 \times 10^{19}$	$M_w 7.14$

of remainder observations in the Ahba block and block V are 246 and 225, respectively. However, the InSAR results only measure the relative motion between two sides of the fault. To make their reference frame same as the GPS data, we averaged the velocities of three GPS stations (H056, H062, and SCLH) on the Xianshuihe fault between Zhuwo and Daofu (Figure 3b) and used the value to correct the InSAR deformation rate map.

## 4. Earthquake Rupture Segment Model and Fault Geometric Model

### 4.1. Earthquake Rupture Segment Model

The spatial and temporal distribution of paleoearthquakes and historical earthquakes shows that the XAZ fault system has distinct segmental characteristics of earthquake rupture. *Wen [2000]* divided the XAZ fault system into 12 rupture segments: 9 for the Xianshuihe fault, 2 (Shimian-Mianning, S7 and Mianning-Xichang, S8; Figure 4) for the Anninghe fault, and 1 (Xichang-Qiaojia, S9) for the Zemuhe fault. In a more recent study of *Wen et al. [2008a]*, two segments located between Bamei and Kangding are removed by taking the three parallel branches as the rupture flower structures of strike-slip fault zones (Figure 4). So the rupture segments of the Xianshuihe fault decreases to 7. According to the field investigation in *Allen et al. [1991]*, the 1893 earthquake near Bamei caused major damage at Songlingkou Pass and the Jinlong Monastery located between Bamei and Selaha. Thus, we treat the two segments from Songlingkou Pass to Bamei and from Bamei to Selaha in *Wen et al. [2008a]* as one single segment and further reduce the Xianshuihe fault into 6 segments (S1–S6) in our inversion scheme. Although the scale of segment ruptures is time or cycle variable for most fault segments and there are only 2–3 segments where the earthquake rupture scale in successive cycles seems to be characteristic [*Wen et al., 2008a*], we still assume that the earthquake occurrence on each segment obeys the characteristic event model [*Schwartz and Coppersmith, 1984*]. This hypothesis is sufficient for exploring the short-term interseismic crust deformation [*Evans et al., 2012*]. The approximate magnitudes and recurrence intervals of characteristic events on these segments are listed in Table 2. The latest earthquakes on 9 segments of the XAZ fault system are presented in Table 3. With this earthquake rupture segment model, we can include the viscoelastic relaxation effect of last earthquakes when inverting the slip deficit rate distribution.

### 4.2. Fault Geometric Model

Based on Chinese active tectonic map [*Deng et al., 2003*], we extract a delicate ground trace for the XAZ fault system (Figure 4). Three branches of the Xianshuihe fault between Bamei and Kangding are simplified to a strip. The northeastern and southwestern branches are omitted. According to the last earthquakes on 6 segments (S1–S6) of the Xianshuihe fault (Table 3), we consider that the Xianshuihe fault dips southwestward. The dip angles of segment groups S1–S3, S4, and S5 and S6 are assumed to be 90°, 85°, and 80°, respectively. However, the deep seismic sounding profiles [*Yang et al., 2011*] and 2-D electrical resistivity structure across the Anninghe fault from magnetotelluric data (J. Cai et al., Crustal electrical structure beneath the southeastern margin of Tibetan Plateau along the profile Muli-Zigong and tectonic implications, *Earth Planets Space*, under review, 2015) indicate that the Anninghe and Zemuhe faults dip eastward. The dip angles of S7 and S8 and S9 are presumed to

**Table 3.** The Last Earthquake Parameters of  $M > 6.5$  Occurred on Nine Segments of the XAZ Fault System

Segment	Date	Magnitude	Epicenter		Rupture Width (km)	Rupture Length (km)	Dip (deg)	Reference
			Latitude (deg)	Longitude (deg)				
S1	06/02/1973	$M_5$ 7.5	31.40	100.60	15	90-110	87	Zhou et al. [1983]
		7.6				90		Allen et al. [1991]
		7.4	31.50	100.24	15	105	87	Papadimitriou et al. [2004]
		7.6	31.50	100.52		90		Wen et al. [2008a]
S2	24/03/1923	7 1/2				>60		Allen et al. [1991]
		7.2	31.30	100.75	15	60	90	Papadimitriou et al. [2004]
		7.3	31.17	100.90		60		Wen et al. [2008a]
S3	23/01/1981	$M_5$ 6.8	31.00	101.20	10	42-46	90	Zhou et al. [1983]
		6.9				44		Allen et al. [1991]
		6.5	31.00	101.20	15	44	85	Papadimitriou et al. [2004]
		6.9	30.95	101.15		45		Wen et al. [2008a]
S4	29/08/1893	≥7				≥40		Allen et al. [1991]
		7.2	30.60	101.50	15	50	85	Papadimitriou et al. [2004]
		7.0	30.70	101.37		70		Wen et al. [2008a]
S5	14/04/1955	7 1/2				27		Allen et al. [1991]
		7.5	30.10	101.80	15	35	81	Papadimitriou et al. [2004]
		7.5	30.03	101.84		35		Wen et al. [2008a]
S6	01/06/1786	7 3/4				70		Allen et al. [1991]
		7.7	29.90	102.00				Papadimitriou et al. [2004]
		7 3/4	29.87	102.04		90		Wen et al. [2008a]
S7	27/09/1480	7 1/2	28.86	102.21		75		Wen et al. [2008a]
S8	29/03/1536	7 1/2	28.23	102.19		80		Wen et al. [2008a]
S9	12/09/1850	7 1/2	27.37	102.53		110		Wen et al. [2008a]

be  $85^\circ$  and  $80^\circ$ , respectively. The rupture depths of last earthquakes are almost  $\sim 15$  km (Table 3). Additionally, the relocated small earthquake distribution in western Sichuan from 1992 to 2002 shows that the depths of hypocenters are mostly less than 15 km [Zhu et al., 2005], which is accordant with the depth profile of  $M > 2.0$  instrumental records along the XAZ fault system [Wen et al., 2008b; Yi et al., 2005]. To obtain more details in the inversion results, we extend the fault width to 20 km. Furthermore, the geometric model of the XAZ fault system (Figure 5) is constructed with TDEs by using the meticulously designed and automatic method to avoid dislocation overlaps and gaps [Jiang et al., 2013]. Through this way, the stress singularity and some other potential negative influences can be inhibited. The size of each TDE patch is about  $18 \text{ km}^2$ , which is confirmed to be a sufficient resolution for stable inversion results.

## 5. New 3-D Viscoelastic Interseismic Coupling Model

In this study, we take into consideration the nonrecoverable homogeneous intrablock strain and elaborate a relatively comprehensive analytical 3-D viscoelastic model (Table 1) to take advantage of the sophisticated fault geometry generated with TDEs. The interseismic crustal velocities  $V_I$  are assumed to result from four tectonic processes: (1) steady state block motion, (2) nonrecoverable homogeneous intrablock strain, (3) slip deficit on fault surface, and (4) viscoelastic relaxation effect of last earthquakes. Moreover, the method of adding extra slip to cancel the fault-normal slip discontinuity on dipping faults introduced by block motion [Johnson and Fukuda, 2010] is incorporated. Therefore, the formula of our model can be represented as

$$V_I = V_B + V_e + V_C + V_L + V_P, \quad (1)$$

where  $V_B$  and  $V_e$  are the interseismic horizontal velocities caused by steady state block rotation and strain. Their detailed expressions for an observation station in block interior can be written as

$$\begin{bmatrix} -r \cos \lambda \sin \varphi & -r \sin \lambda \sin \varphi & r \cos \varphi \\ r \sin \lambda & -r \cos \lambda & 0 \end{bmatrix} \begin{bmatrix} \omega_x \\ \omega_y \\ \omega_z \end{bmatrix} + \begin{bmatrix} r \Delta\lambda \cos \varphi & 0 & r \Delta\varphi / 2 \\ 0 & r \Delta\varphi & r \Delta\lambda \cos \varphi / 2 \end{bmatrix} \begin{bmatrix} \dot{\epsilon}_x \\ \dot{\epsilon}_y \\ \dot{\gamma}_{xy} \end{bmatrix}, \quad (2)$$

according to Savage et al. [2001], where  $r$  is the Earth radius,  $(\lambda, \varphi)$  are the coordinates of the observation point,  $\Delta\lambda$  and  $\Delta\varphi$  are the differences of longitude and latitude, respectively, from the block centroid, and  $(\omega_x, \omega_y, \omega_z)$

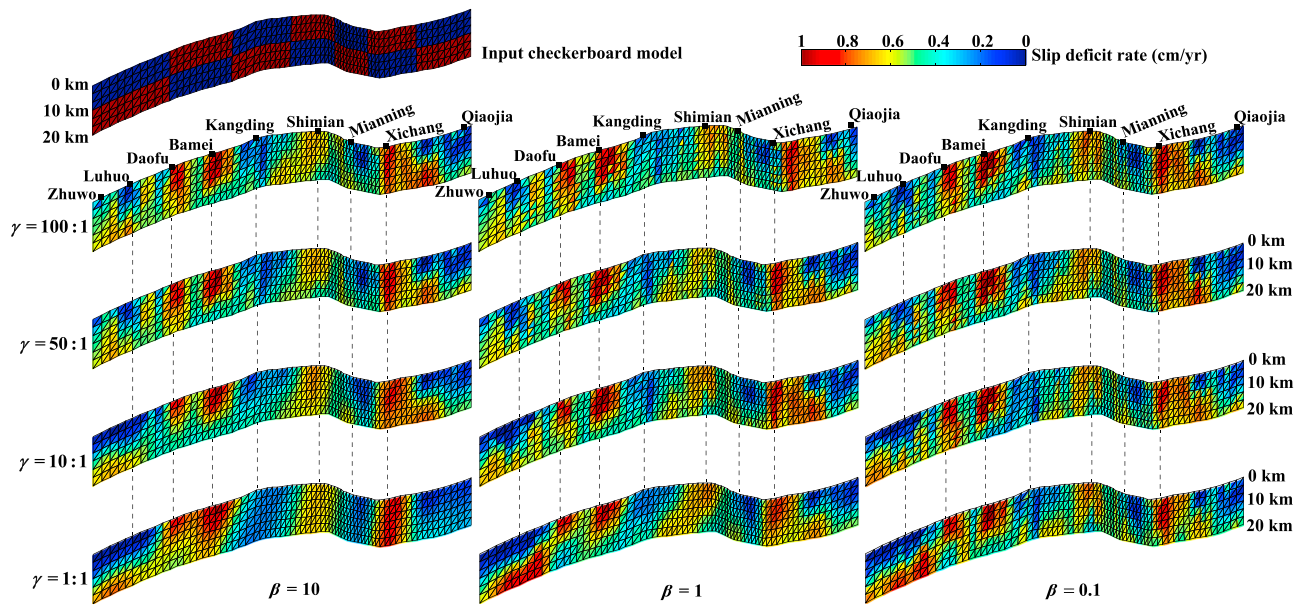


**Figure 5.** The input fault coupling model for synthetic validation and the resulting slip deficit rate distributions with different weight ratios and smoothing factors.

are the Euler vector of block rotation.  $\dot{\epsilon}_x$ ,  $\dot{\epsilon}_y$ , and  $\dot{\epsilon}_{xy}$  are the strain rate tensor components.  $V_C$  represents the velocities from the extra tensile slip introduced for the steady state velocity field, which can be calculated as

$$G_C s_C = G_C \begin{bmatrix} 0 & 1/\cos \delta - \cos \delta \\ 0 & -\sin \delta \end{bmatrix} \begin{bmatrix} s_{\parallel} \\ s_{\perp} \end{bmatrix}, \quad (3)$$

where  $G_C$  is a Green's function matrix calculated from the angular dislocation model in an elastic half-space [Comninou and Dundurs, 1975]. Parameter  $s_C$  denotes the slip discontinuity compensation. Parameter  $\delta$  is the fault dip angle. The  $s_{\parallel}$  and  $s_{\perp}$  are the steady long-term strike-slip and tensile-slip components introduced by the rigid rotation and permanent strain of two adjacent blocks. Their expressions can be written as the velocity differences between the hanging wall and footwall blocks:

$$\begin{bmatrix} s_{\parallel} \\ s_{\perp} \end{bmatrix} = \begin{bmatrix} \sin \alpha & \cos \alpha \\ \cos \alpha & \sin \alpha \end{bmatrix} \begin{bmatrix} G_B^h & G_e^h & -G_B^f & -G_e^f \end{bmatrix} \begin{bmatrix} \Omega^h \\ \dot{\epsilon}^h \\ \Omega^f \\ \dot{\epsilon}^f \end{bmatrix}, \quad (4)$$

where  $\alpha$  is the strike of fault. The right subscript “B” and “e” remark the Green's function matrices of block rotation and strain, respectively (equation (2)).  $V_L$  and  $V_P$  denote the surface velocities caused by slip deficit  $s_L$  and postseismic viscoelastic relaxation, respectively. The Green's functions for slip deficit and postseismic effect are both from the mathematical formulations of quasi-static displacements for dislocations in a multilayered elastic-viscoelastic half-space under gravity, which are derived from the associated elastic solutions by using the consistency principle of linear viscoelasticity [Fukahata and Matsu'ura, 2005, 2006].

For the InSAR data, an overall linear offset correction, which may exist between the observations and the model results, should be added into the right side of equation (1) to eliminate the residual orbit errors. The readers can refer to Jiang *et al.* [2013] for the concrete expressions of the linear correction item. Additionally, to avoid large fluctuations in slip deficit rates between adjacent patches, a smoothing constraint,

$$0 = \beta \nabla^2 s_L, \quad (5)$$

is imposed on the distribution of slip deficit rates. Parameter  $\beta$  is the smoothing parameter.  $\nabla^2$  is the scale-dependent umbrella smoothing operator used in the inversions for TDE slip distribution [Desbrun *et al.*, 1999; Maerten *et al.*, 2005].

**Table 4.** The Rotation and Strain Parameters of Five Blocks in Synthetic Validation

Style	Block	$\omega_x$ ( $10^{-8}$ /yr)	$\omega_y$ ( $10^{-8}$ /yr)	$\omega_z$ ( $10^{-8}$ /yr)	$\varepsilon_x$ ( $10^{-8}$ /yr)	$\dot{\varepsilon}_y$ ( $10^{-8}$ /yr)	$\dot{\gamma}_{xy}$ ( $10^{-8}$ /yr)
Input parameters	I	8.239	-39.367	-9.811	-2.243	1.725	-0.870
	II	-5.695	7.716	12.374	-3.072	0.717	0.612
	III	-3.899	8.976	6.872	-0.788	0.262	1.541
	IV	-15.409	20.235	17.521	-0.039	-1.018	2.024
	V	9.337	-110.970	-49.309	-1.983	2.098	2.410
Resulting parameters	I	$8.466 \pm 0.977$	$-40.554 \pm 5.6469$	$-10.619 \pm 3.754$	$-2.213 \pm 0.175$	$1.727 \pm 0.150$	$-0.821 \pm 0.220$
	II	$-6.742 \pm 2.866$	$12.557 \pm 12.795$	$15.406 \pm 8.132$	$-3.129 \pm 0.401$	$0.620 \pm 0.398$	$0.829 \pm 0.521$
	III	$-3.990 \pm 0.526$	$9.315 \pm 2.215$	$7.065 \pm 1.272$	$-0.780 \pm 0.071$	$0.254 \pm 0.046$	$1.548 \pm 0.083$
	IV	$-15.162 \pm 1.056$	$18.865 \pm 4.935$	$16.849 \pm 2.504$	$0.028 \pm 0.191$	$-1.040 \pm 0.094$	$1.970 \pm 0.215$
	V	$9.592 \pm 1.119$	$-112.370 \pm 5.963$	$-50.143 \pm 3.449$	$-2.019 \pm 0.186$	$2.095 \pm 0.130$	$2.442 \pm 0.236$

In our 3-D viscoelastic interseismic deformation model, the steady state long-term slip can be obtained from

$$\mathbf{s} = \begin{bmatrix} 1 & 0 \\ 0 & 1/\cos \delta \end{bmatrix} \begin{bmatrix} s_{\parallel} \\ s_{\perp} \end{bmatrix}. \quad (6)$$

The locked slip deficit rate is obtained directly from the inversions of geodetic observations. We do not prescribe any relationship between them. The steady state long-term slip is prescribed to be the superposition of interseismic fault creep and slip deficit. Therefore, the interseismic fault creeping rates can be derived from the slip deficit rates and the steady state long-term slip rates as  $s - s_L$ . For an ideal earthquake cycle model, the coseismic slip of an episodic earthquake is equal to  $Ts_L$ , where  $T$  is the earthquake recurrence interval. As in *Johnson and Fukuda [2010]*, the fault is not prescribed to be fully locked above a constant depth. Rather, the fault has a finite width and is equally discretized with TDEs. During the interseismic period, each TDE is considered to be either fully or partially locked. The interaction of two adjacent blocks on the boundary fault can be quantified by a purely kinematic scalar coefficient  $\phi$ ,

$$\phi = \sqrt{\frac{(\mathbf{s}_L)^T \mathbf{s}_L}{\mathbf{s}^T \mathbf{s}}}, \quad (7)$$

which is named as the coupling ratio. During the interseismic period, if  $\phi = 0$ , fault creeps at the long-term steady slip rate. And if  $\phi = 1$ , no creep occurs on the fault interface. However, in most cases, the coupling ratio is  $0 < \phi < 1$ , which indicates fault creeps at a rate lower than  $s$  and accumulates seismic energy.

## 6. Geodetic Inversions

### 6.1. Synthetic Validation

To determine the optimal weight proportion  $\gamma$  of GPS observations with respect to InSAR observations and the optimal smoothing constant in our viscoelastic model (equation (5)), we first conduct inversions of synthetic data before the formal inversions of real data. The surface velocities at the observation stations are modeled by using the synthetic rotation and strain parameters of five blocks (Table 4) and the checkerboard distribution of slip deficit rates (Figure 5). The sizes of checkerboard patches are approximately  $130 \text{ km} \times 10 \text{ km}$  with alternative coupling rates from  $0 \text{ mm/yr}$  to  $10 \text{ mm/yr}$ . During the simulations, the uncertainties of the GPS and InSAR observations are imposed on the predicted velocities. Additionally, the viscosity is prescribed to be  $10^{18} \text{ Pa s}$  with known earthquake timing parameters (Tables 2 and 3) such that the viscoelastic Green's functions need not to be computed repeatedly.

We use the Monte Carlo method and the bounded variable least squares algorithm [*Stark and Parker, 1995*] to carry out the synthetic inversions. In total, 100 disturbed data sets are generated by adding the sampled observation noises to the synthetic data. The inversion results (Figure 5) show that the recovered coupling distributions vary with the weight ratio  $\gamma$  and the smoothing constant  $\beta$ . The decreasing ratios improve the spatial resolution of recovered slip deficit distribution especially below Zhuwo and Luhuo without negative effects on the other segments of the XAZ fault system. When  $\gamma$  is equal to 1, the recovered coupling distributions approximate the input model best, which implies that the InSAR data used in our viscoelastic model provide strong constraints on the slip deficit rates of the fault segment they covered. Additional

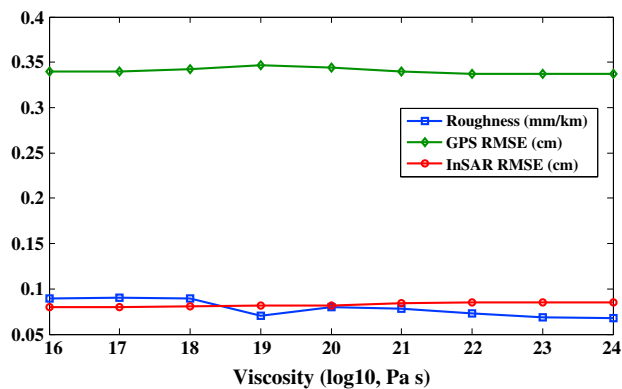


**Figure 6.** The fitness to geodetic observations and the roughness of slip deficit rate distributions with increasing viscosities.

low smoothing value of  $\beta = 0.1$ , the outlines of alternating checkerboard patches are ambiguous. As a compromise, we choose a smoothing value of 1 with the optimal weight ratio for real data inversions to capture along-strike coupling variations.

## 6.2. Inversion Results

Under the fixed weight ratio and smoothing factor, we invert the rotation and strain parameters of five blocks and slip deficit rate distributions with increasing viscosities from  $10^{16}$  Pa s to  $10^{24}$  Pa s, which is wider than the published range. The results show that different viscosities have little influence on the fitness to GPS and InSAR observations and the roughness of slip deficit distribution (Figure 6), implying that geodetic data itself are not sufficient to provide a strong constraint for determining the viscosity of crust flow. Also, it reveals that, compared with the approach of determining the viscosity of lower crust from postseismic deformation, the way of interseismic deformation is more difficult. Here we present the coupling distributions of four probable viscosities (Figure 7). Their maximum slip deficit rates are all  $\sim 12.7$  mm/yr. The slip deficit rates on most of fault patches are  $\sim 4$  mm/yr.

There are five consistent large concentration zones of high slip deficit rates among these four resulting distributions, one between Zhuwo and Luhuo, one below Kangding, two between Mianning and Xichang, and one at Qiaojia, although their sizes are not identical. However, the high slip deficit rate patches at the bottom of the Xianshuhe fault between Luhuo and Bamei in Figures 7a–7c are absent in Figure 7d. And the high slip deficit-concentrated zone between Shimian and Mianning in Figures 7a, 7c, and 7d also disappears in Figure 7b. It probably indicates that the near-fault observations at these places are not enough to provide a unique inversion result. We can get another proof from Figure 5, where the color of the recovered checkerboard near Shimian from depth of 0 km to 10 km is obviously lighter than other red checkerboards above the depth of 10 km ( $\gamma = 1, \beta = 1$ ). Table 5 lists the resulting rotation and strain parameters of five blocks. The variation in these values is obscure, and the fluctuation in the strain parameters is less than the rotation parameters. These show that the GPS observations can provide good constraints on the block parameters but are not sufficient to reveal subtle interseismic faulting features, which need more observations in the width of double locking depth near the fault.

Taking the interseismic deformation model of  $10^{18}$  Pa s (Figure 7a) as an example, we model the geodetic observations. The predicted GPS velocities are delineated in Figure 3a with gray arrows. Almost all the residual GPS velocities are encompassed in the error ellipses of 95% confidence (Figure 8a). The statistical results show that 91.5% of residuals are lower than 2.5 mm/yr. The average value is only 1.3 mm/yr. The maximum value of the residuals is 8.1 mm/yr. Four GPS stations in the InSAR coverage with large residuals are labeled in Figure 8a. Among them, the stations H056, SCLH, and H062 on the XAZ fault system are used to correct the InSAR rate map. Due to the least deviation of the velocity on SCLH from the average value than the values on H056 and H062, the fitting residual on this station is the lowest. The fitness on the other stations in the InSAR area except H039 is as good as that in other regions. Figure 3a shows that the velocity on H039 is distinctly lower than the surrounding stations. For the InSAR data, the maximum residual range change rate is 2.6 mm/yr. The mean residual is only 0.6 mm/yr. The 77.5% of the residuals are less than 0.8 mm/yr.

comparisons of resulting rotation and strain parameters of five blocks show that they primarily depend on the widely dispersed GPS observations instead of the near-fault InSAR observations.

However, decreasing smoothing factor  $\beta$  does not always enhance the spatial resolution of recovered coupling distribution. Above the depth of  $\sim 10$  km, the resolution shows a trend of deterioration for a fixed weight ratio. Below the depth of  $\sim 10$  km, the opposite is the case. On the other hand, the boundaries of checkerboards become more and more sharp with the decreasing  $\beta$ . At the

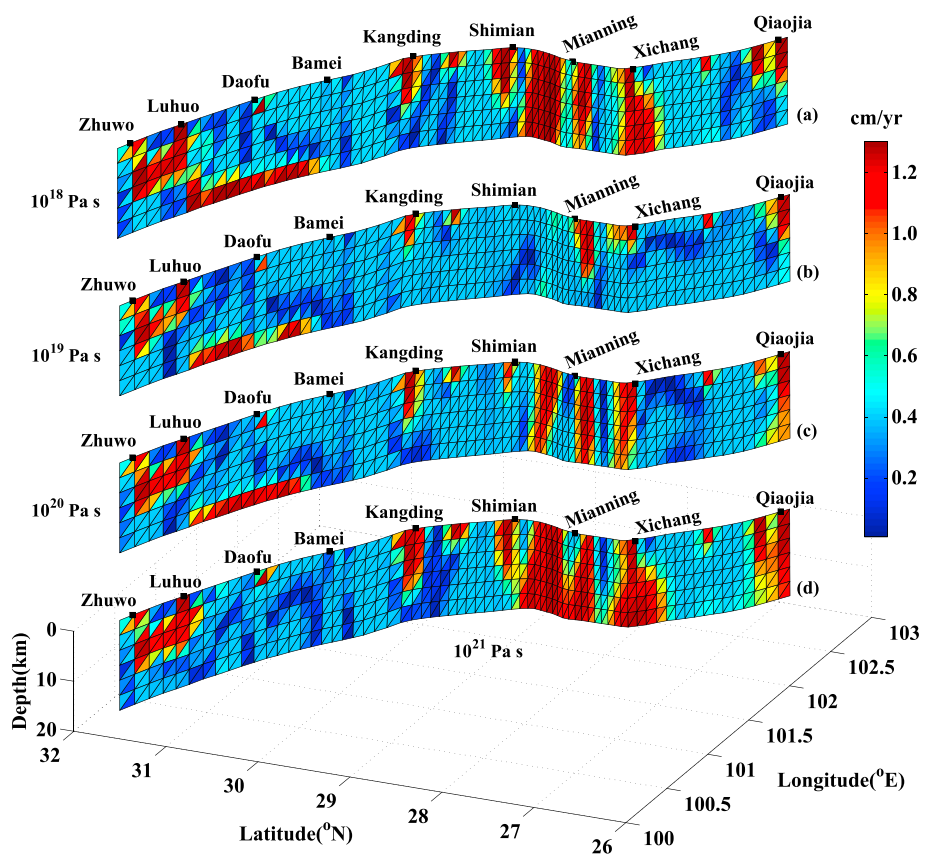


**Figure 7.** (a–d) Four slip deficit rate distributions of different viscosities from the joint inversions of GPS and InSAR observations.

**Table 5.** The Rotation and Strain Parameters of Five Blocks Inferred From GPS and InSAR Observations With Different Viscosities

Block	Viscosity	$\omega_x (10^{-8}/\text{yr})$	$\omega_y (10^{-8}/\text{yr})$	$\omega_z (10^{-8}/\text{yr})$	$\varepsilon_x (10^{-8}/\text{yr})$	$\dot{\varepsilon}_y (10^{-8}/\text{yr})$	$\dot{\gamma}_{xy} (10^{-8}/\text{yr})$
I	$10^{18} \text{ Pa s}$	$5.895 \pm 0.966$	$-26.002 \pm 5.566$	$-0.147 \pm 3.701$	$-1.759 \pm 0.167$	$1.318 \pm 0.153$	$-2.197 \pm 0.222$
	$10^{19} \text{ Pa s}$	$6.433 \pm 1.001$	$-29.494 \pm 5.596$	$-2.600 \pm 3.727$	$-1.742 \pm 0.164$	$1.236 \pm 0.172$	$-2.186 \pm 0.251$
	$10^{20} \text{ Pa s}$	$6.155 \pm 1.061$	$-28.159 \pm 6.079$	$-1.603 \pm 4.032$	$-1.765 \pm 0.184$	$1.301 \pm 0.176$	$-2.122 \pm 0.289$
	$10^{21} \text{ Pa s}$	$6.957 \pm 0.890$	$-32.716 \pm 4.901$	$-4.728 \pm 3.294$	$-1.692 \pm 0.166$	$1.132 \pm 0.163$	$-2.141 \pm 0.261$
II	$10^{18} \text{ Pa s}$	$-12.125 \pm 2.640$	$35.651 \pm 11.773$	$29.909 \pm 7.472$	$-2.093 \pm 0.393$	$0.589 \pm 0.392$	$1.492 \pm 0.485$
	$10^{19} \text{ Pa s}$	$-11.579 \pm 2.329$	$31.936 \pm 10.401$	$27.680 \pm 6.549$	$-2.342 \pm 0.362$	$0.633 \pm 0.432$	$1.245 \pm 0.475$
	$10^{20} \text{ Pa s}$	$-13.912 \pm 2.389$	$43.436 \pm 10.660$	$34.739 \pm 6.752$	$-2.068 \pm 0.380$	$0.392 \pm 0.389$	$1.618 \pm 0.462$
	$10^{21} \text{ Pa s}$	$-11.881 \pm 2.228$	$34.752 \pm 10.007$	$29.373 \pm 6.328$	$-2.018 \pm 0.336$	$0.536 \pm 0.424$	$0.977 \pm 0.462$
III	$10^{18} \text{ Pa s}$	$-3.844 \pm 0.536$	$5.851 \pm 2.199$	$8.411 \pm 1.267$	$-0.006 \pm 0.073$	$0.246 \pm 0.043$	$0.907 \pm 0.081$
	$10^{19} \text{ Pa s}$	$-6.236 \pm 0.484$	$14.635 \pm 2.119$	$13.227 \pm 1.184$	$-0.075 \pm 0.068$	$0.203 \pm 0.043$	$1.048 \pm 0.080$
	$10^{20} \text{ Pa s}$	$-5.465 \pm 0.487$	$11.482 \pm 2.169$	$11.516 \pm 1.189$	$-0.050 \pm 0.066$	$0.296 \pm 0.048$	$0.917 \pm 0.077$
	$10^{21} \text{ Pa s}$	$-3.772 \pm 0.511$	$4.830 \pm 2.198$	$7.981 \pm 1.260$	$-0.004 \pm 0.068$	$0.271 \pm 0.043$	$0.781 \pm 0.074$
IV	$10^{18} \text{ Pa s}$	$-4.440 \pm 1.127$	$-33.142 \pm 5.312$	$-8.368 \pm 2.684$	$1.049 \pm 0.194$	$-1.356 \pm 0.092$	$3.184 \pm 0.253$
	$10^{19} \text{ Pa s}$	$-2.650 \pm 1.302$	$-39.666 \pm 6.146$	$-11.703 \pm 3.085$	$0.923 \pm 0.205$	$-1.279 \pm 0.087$	$2.731 \pm 0.229$
	$10^{20} \text{ Pa s}$	$-3.865 \pm 1.167$	$-33.940 \pm 5.526$	$-8.953 \pm 2.798$	$0.991 \pm 0.166$	$-1.272 \pm 0.096$	$2.975 \pm 0.216$
	$10^{21} \text{ Pa s}$	$-3.668 \pm 1.136$	$-35.581 \pm 5.366$	$-9.517 \pm 2.701$	$0.988 \pm 0.210$	$-1.351 \pm 0.088$	$3.101 \pm 0.221$
V	$10^{18} \text{ Pa s}$	$6.189 \pm 1.006$	$-98.466 \pm 5.283$	$-40.031 \pm 3.083$	$-3.221 \pm 0.183$	$2.108 \pm 0.131$	$3.240 \pm 0.217$
	$10^{19} \text{ Pa s}$	$6.786 \pm 0.895$	$-98.716 \pm 4.461$	$-40.816 \pm 2.612$	$-3.439 \pm 0.150$	$1.952 \pm 0.116$	$3.330 \pm 0.216$
	$10^{20} \text{ Pa s}$	$6.385 \pm 0.851$	$-97.762 \pm 4.146$	$-40.089 \pm 2.432$	$-3.387 \pm 0.167$	$2.012 \pm 0.130$	$3.463 \pm 0.197$
	$10^{21} \text{ Pa s}$	$6.669 \pm 0.913$	$-99.753 \pm 4.696$	$-40.739 \pm 2.761$	$-3.187 \pm 0.170$	$1.892 \pm 0.115$	$3.285 \pm 0.190$

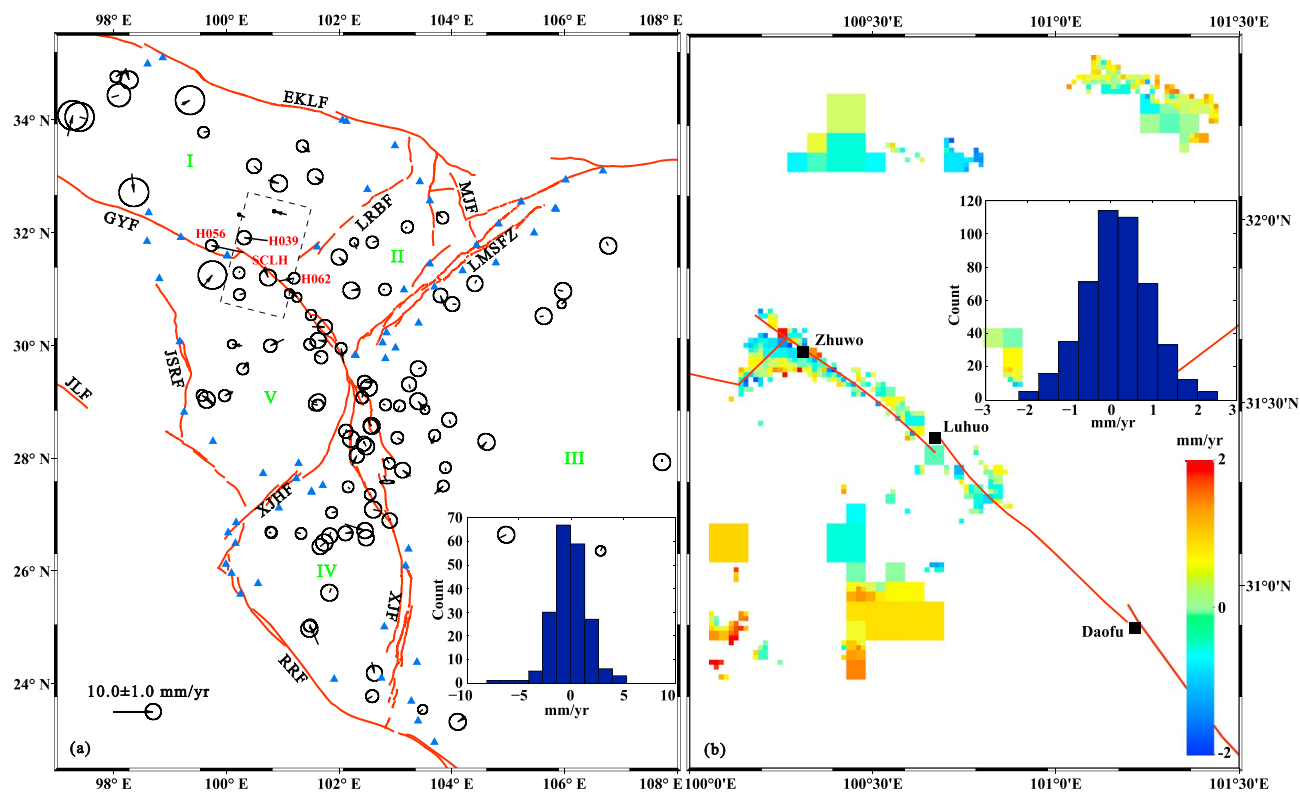


**Figure 8.** Residual GPS velocities and InSAR deformation rate map from the interseismic deformation model of  $10^{18}$  Pa s. (a and b) Their statistical histograms are embedded, respectively. The error ellipses in Figure 8a represent 95% confidence.

### 6.3. Resolution Tests

To determine the minimum along-strike wavelength that geodetic observations can resolve, we decrease the size of checkerboard from  $\sim 130$  km to  $\sim 26$  km and carry out more synthetic validations with the fixed weight ratio and smoothing constant in the case of  $10^{18}$  Pa s. The synthetic inversion results show that above the depth of  $\sim 10$  km, all the checkerboards in Figures 9a and 9b can be distinguished. In Figure 9c, the checkerboards from Zhuwo to Kangding and from Mianning to Qiaojia can be identified. In Figure 9d, the checkerboards from Zhuwo to Daofu and from Bamei to Kangding and below Qiaojia can be recovered. Below the depth of  $\sim 10$  km, the spatial resolution of coupling distribution is poor and lower than above. However, the S1 segment (almost from Zhuwo to Luhuo) of the Xianshuihe fault is an exception. The alternating checkerboard pattern on this segment is recovered best from 0 km to 20 km, which benefits from the strong constraints of near-fault InSAR observations.

Above the depth of  $\sim 10$  km, the resolution tests show that we are able to recover the locking features ranging from 39 km to 52 km in the along-strike wavelength between Kangding and Mianning (Figures 9a–9c). The minimum length of locking features between Daofu and Bamei and between Mianning and Qiaojia that can be resolved is between 26 km and 39 km. The minimum resolvable wavelengths between Zhuwo and Daofu and between Bamei and Kangding can reach up to  $\sim 26$  km, maybe even shorter. For the five similar high slip deficit-concentrated zones in Figure 7, the length of the feature between Zhuwo and Luhuo is  $\sim 65$  km. The length of the feature near Kangding is  $\sim 39$  km. The lengths of other three features between Mianning and Qiaojia are between 39 and 52 km. The lengths of these five features are absolutely longer than the minimum resolvable wavelengths of corresponding segments, which guarantees the existence of these five high slip deficit-concentrated zones at least above  $\sim 10$  km depth.

## 7. Discussion

### 7.1. Comparison With Published Slip Rates

Using the slip deficit rate distribution model of  $10^{18}$  Pa s, as well as the resulting rotation velocities and strain rates of five blocks (Table 5), we calculate the steady long-term slip rates on the XAZ fault system (Figure 10a).

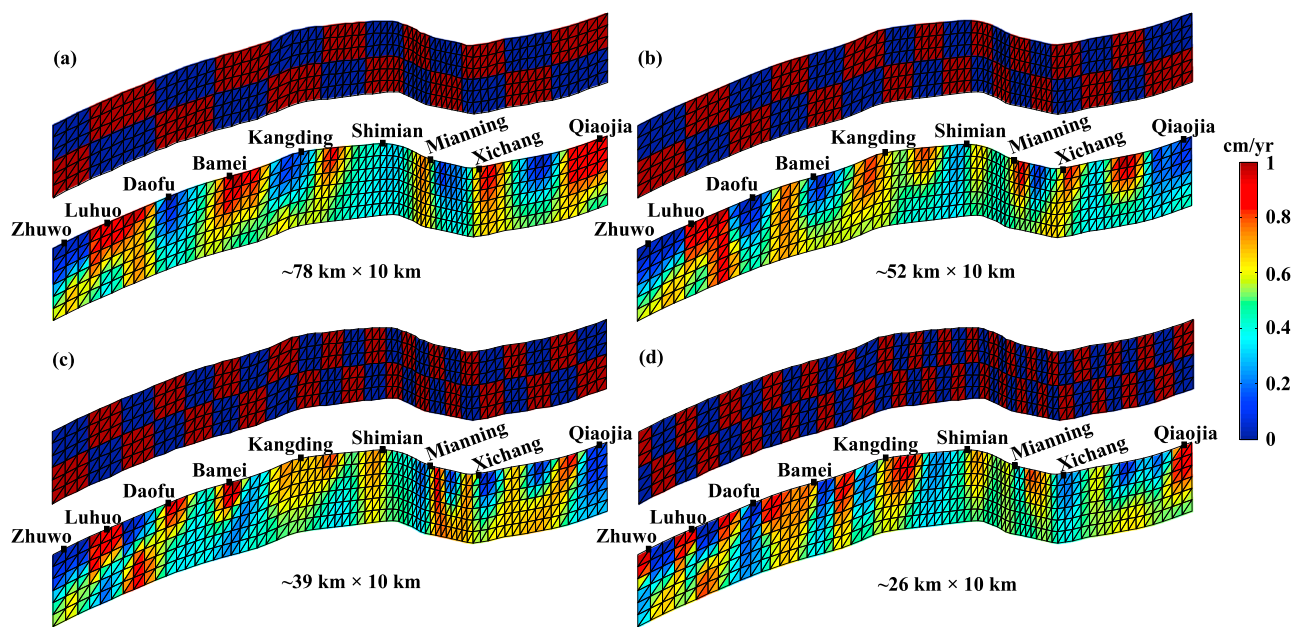


**Figure 9.** (a–d) Resolution testing results with decreasing checkerboard lengths. The viscosity is assigned to be  $10^{18} \text{ Pa s}$ . Both the weight ratio and the smoothing factor are fixed at 1.

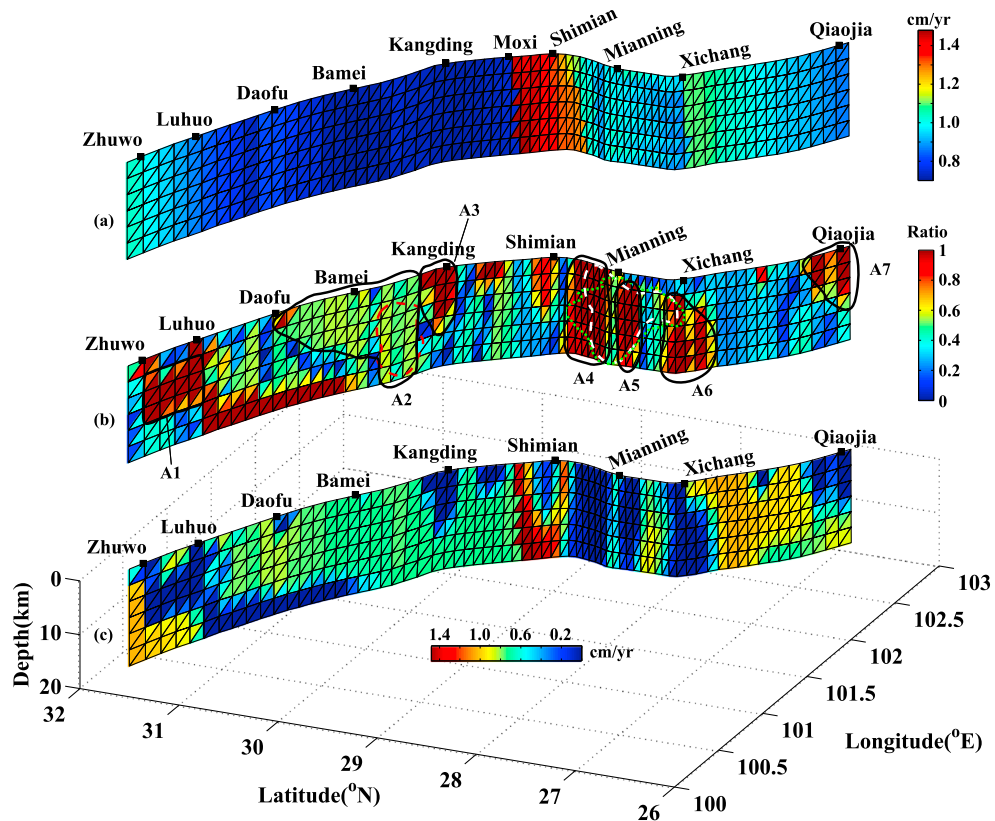


**Figure 10.** (a) Estimated long-term slip rate distribution on the XAZ fault system. (b) The coupling ratio distribution calculated from the distribution model of  $10^{18} \text{ Pa s}$ . Seven potential asperities are outlined with the black lines. The red dashed line delimits the scope of the locking asperity in *Yi et al.* [2005]. The white and green lines are the outlines of the locking asperities in *Yi et al.* [2004] and *Wen et al.* [2008b], respectively. (c) Referential interseismic fault creep distribution.

**Table 6.** The Geological and Geodetic Slip Rates of the XAZ Fault System (Unit: mm/yr)

Source	Xianshuihe Fault						Anninghe Fault		Zemuhe Fault
	S1	S2	S3	S4	S5	S6	S7	S8	S9
Geological rates	<i>Allen et al. [1991]</i>	15 ± 5				~5			
	<i>Chen et al. [2008]</i>			17 ± 3	6.7 ± 3	7.9 ± 1.5 and 9.1 ± 2	7.3 ± 2		
	<i>Zhang [2013]</i>				~10.2, ~10.4, and ~9.3		5.0 ± 1.2		~6.7
	<i>Xu et al. [2003]</i>					9.6 ± 1.7	6.5 ± 1		6.4 ± 0.6
Geodetic rates	<i>Shen et al. [2005]</i>	10 ± 2		10 ± 2		11 ± 2	4 ± 2		7 ± 2
	<i>Wang et al. [2009]</i>	9~12				10 ± 1.5		~5	
	<i>Zhang [2013]</i>		9.0 ± 1.5						5.5 ± 1.5
	This study	8.7~10.3	7.7~8.8	7.3~8.3	7.1~7.6	7.0~7.4	7.2~14.7	9.1~12.9	8.8~11.1
									8.7~10.9

The slip rate ranges of the 9 segments are documented in Table 6. The minimum slip rate is 7.0 mm/yr near the north of Bamei. The maximum value is 14.8 mm/yr near the center of the Kangding-Shimian segment (S6 in Figure 4), and at the Moxi town, which can be taken as the demarcation of the minimum and maximum rates. From here, the slip rates almost increase northward and decline southward, respectively. Additionally, this place is also at the junction of the XAZ fault system and the Longmenshan fault, which is the boundary of the adjacent Longmengshan subblock and south China block. The eastern transition velocities of the Sichuan-Yunnan terrace, Longmenshan subblock, and south China block are  $13.72 \pm 1.6$  mm/yr,  $7.68 \pm 1.58$  mm/yr, and  $6.36 \pm 1.65$  mm/yr, respectively [Shen et al., 2005]. The larger velocity difference of eastern transition between the Sichuan-Yunnan terrace and south China block, compared with the Longmenshan subblock, is probably the reason of the distinct demarcation near the Moxi town.

In the past decades, both geological and geodetic studies have reported the Holocene and present-day slip rates of the XAZ fault system (Table 6). For the Xianshuihe fault, the geological rates of the northern four segments (S1–S4) are larger than our results, except the other two segments (S5 and S6). The decline trend of the slip rates along the Xianshuihe fault from northwest to south in *Allen et al. [1991]* can also be found here. Besides, the slip rate jump near the Moxi town is also discovered in the geological investigation of *Chen et al. [2008]*, although the step is smaller in their study. From Table 6, we can see that our long-term slip rates are close to, but a little lower than, published decadal rates, which can probably be attributed to the postseismic viscoelastic relaxation considered in our model. The relaxation time of the middle lower crust mantle with the viscosity of  $10^{18}$  Pa s is ~20 years under a rigidity of 30 GPa. The elapsed time of last earthquakes on the segments of S1, S3, and S5 is ~40, 30, and 60 years, respectively. Both the relaxation time and the elapsed time are much less than the recurrence intervals of these three segments. As suggested by *Johnson and Fukuda [2010]*, the crustal velocities are greater than the long-term plate motion rates in early stage of a seismic cycle, when the earthquake recurrence time is longer than the relaxation time of underlying viscoelastic substratum.

For the Anninghe and Zemuhe faults, the published GPS slip rates are lower than the Holocene rates, which are still less than our results for ~2 mm/yr. The observation time of geodetic data is in the late stage of the earthquake cycles of S7 and S8. In contrast to the case being early in an earthquake cycle, the ground velocities are less than the plate motion rates in the late cycle, which is a probable cause for our high slip rates. In addition, the modeling approach of the steady state long-term slip is another possible cause. The published GPS rates listed in Table 6 are only the strike-slip rates without the tensile components, which have been converted to the dip slip in our study by using equation (6).

## 7.2. Asperity Model of the XAZ Fault System

We take the distribution model of  $10^{18}$  Pa s as a reference to locate the potential asperities on the XAZ fault system. In fact, the differences among the four slip deficit rate distributions in Figure 7 are not great, except that an area of high slip deficit between Shimain and Mianning is missing in Figure 7b. More near-fault observations are necessary to testify its existence. We calculate the coupling ratio distribution (Figure 10b) by dividing the slip deficit rates with the long-term rates. The results show high similarity to the model of Figure 7a. The zones with high slip deficit rates are, namely, the high coupling zones, which indicate high strain

**Table 7.** The Depth Ranges and Areas of Seven Potential Asperities

Asperity	A1	A2	A3	A4	A5	A6	A7
Depth range (km)	3.5~13	0~20	0~11	0~20	3.5~20	3.5~20	0~11
Area ( $\text{km}^2$ )	~430	~1620	~280	~1230	~500	~610	~320

accumulation in the interseismic period. So these zones are the potential seismogenic asperities. Figure 10b shows six distinct locking asperities, one between Zhuwo and Luhuo (A1), one near Kangding (A3), one between Shimian and Mianning (A4), two between Mianning and Xichang (A5 and A6), and one at Qiaojia (A7). Their coupling ratios are all close to 1. Besides, from Daofu to Kangding, there is another large region (A2) with coupling ratios between 0.5 and 0.6, which indicates that the patches in this region are able to creep at a lower rate than the long-term rates in the interseismic stage and rupture in future earthquakes. Table 7 lists the depth ranges and areas of these seven asperities.

The locked asperity inferred from the depth profile of microearthquakes between 1981 and 2003 between Daofu and Shimian is situated in the extent of A2 (Figure 10b) [Yi *et al.*, 2005]. In addition, two published microearthquake depth profiles between 1981 and 2006 on the Anninghe and Zemuhe faults show another large-scale potential asperity between Shimian and Xichang [Wen *et al.*, 2008b; Yi *et al.*, 2004]. They provide a support for the large potential asperity A4 on the Shimian-Mianning segment (S7), which is an uncertainty unresolved from geodetic data used in our study. The length of A4 is also longer than the minimum resolvable wavelength between Shimian and Mianning. And their results exclude the possibility of  $10^{19}$  Pa s for the crustal flow in eastern Tibetan Plateau. Due to lack of other evidences, the two asperities between Kangding and Shimian in Figures 7a and 7d, which are not distinct in the cases of  $10^{19}$  Pa s and  $10^{20}$  Pa s, are not considered in our study.

### 7.3. Implication for Seismic Potential

The elapsed time of last earthquakes on the S1 and S5 segments of the Xianshuihe fault is short. However, both of them have distinct asperities (A1 and A3) (Figure 10b). Especially, for the S1 segment, the asperity A1 can be well constrained for the whole depth of 20 km by the abundant near-fault InSAR data. This reveals a fast coupling speed after earthquakes on these two segments, which is probably a reason for their short recurrence intervals of about 200 years.

According to the slip deficit rates in Figure 7b, we calculate the accumulation of seismic moments on the 9 segments of the XAZ fault system by assuming a rigidity of 30 GPa (Table 2). Among them, benefiting from the InSAR data, the reliability of the seismic moment accumulation rate and gross on the S1 segment is the best. The values on the other segments are not as reliable as above, because the slip deficit rates below the depth of 10 km have some uncertainties due to sparse near-fault observations. In general, the accumulation rate on the Zemuhe fault is the highest due to its large scale. However, this fault still has large interseismic creeping rates up to  $\sim 7$  mm/yr (Figure 10c), which is probably the reason of long recurrence interval of  $\sim 2000$  years. The moment accumulation rate of the S3 segment is the lowest. The cumulative moment on the Shimian-Mianning segment (S7) since the last earthquake exceeds the magnitude of the characteristic earthquake, which implies that the asperity A4 on this segment has probably accumulated sufficient strain. And the cumulative moments on the Songlinkou-Selaha (S4) and Mianning-Xichang (S8) segments are very close to the magnitudes of the characteristic earthquakes. In November 2014, two earthquakes occurred on the Selaha-Kangding segment (S5) at the depth of 9 km (Figure 1). Their U.S. Geological Survey magnitudes are  $M_w 5.9$  and  $M_w 5.6$ , respectively, equivalent to a seismic moment of  $1.18 \times 10^{18}$  N m, which is far less than the accumulated moment. The seismic risk of this segment has not been released completely.

## 8. Conclusion

We have presented a comprehensive 3-D viscoelastic interseismic deformation model to infer the long-term rotation and strain rates of fault-bounded blocks and the interseismic fault slip deficit rates from geodetic data. The joint inversions of GPS and InSAR velocities provide spatially variable slip deficit rate distributions for exploring the interseismic behavior and seismic hazards of the XAZ fault system. The widely dispersed GPS data exert strong constraints on the parameters of block motion. However, the near-fault InSAR measurements only reflect the interseismic coupling variations on the S1 segment of the Xianshuihe fault. The observations near Shimian are not enough to present a good spatial resolution for the whole modeled depth.

Different viscosities have little influence on the agreement between model and geodetic observations except for the resulting distribution models. Hence, these geodetic data cannot constrain the viscosity of crustal flow in the eastern Tibetan Plateau. Much more interseismic observations are needed to determine the viscosity than the method of postseismic deformation analysis. Six potential fully coupling asperities, one between Zhuwo-Luhuo, one below Kangding, one between Shimian and Mianning, two between Mianning and Xichang, and one at Qiaojia, are identified along the XAZ fault system. And from Daofu to Kangding, there is another large-scale partially coupling zone with a length over 140 km. Their lengths along the fault strike can be resolved by using currently available geodetic data. The calculated seismic moment accumulations, although with limited confidence, indicate that the Songlinkou-Selaha (S4), Shimian-Mianning (S7), and Mianning-Xichang (S8) segments are in a very high risk of rupture.

#### Acknowledgments

We thank Paul Tregoning, Associate Editor Yan Jiang, and an anonymous reviewer for their suggestions that have helped to improve the presentation of this manuscript. This study is supported by the Basic Scientific Funding of Institute of Geology, China Earthquake Administration (JB-14-03), the National Natural Science Foundation of China (41404012 and 41372221), and the China Postdoctoral Science Foundation (2014 M560102).

#### References

- Allen, C., Z. Luo, H. Qian, X. Wen, H. Zhou, and W. Huang (1991), Field study of a highly active fault zone: The Xianshuihe fault of southwestern China, *Geol. Soc. Am. Bull.*, **103**, 1178–1199.
- Bai, D. H., et al. (2010), Crustal deformation of the eastern Tibetan Plateau revealed by magnetotelluric imaging, *Nat. Geosci.*, **3**, 358–362.
- Béjar-Pizarro, M., A. Socquet, R. Armijo, D. Carrizo, J. Genrich, and M. Simons (2013), Andean structural control on interseismic coupling in the North Chile subduction zone, *Nat. Geosci.*, **6**, 462–467.
- Bell, M. A., J. R. Elliott, and B. E. Parsons (2011), Interseismic strain accumulation across the Manyi fault (Tibet) prior to the 1997  $M_w$ 7.6 earthquake, *Geophys. Res. Lett.*, **38**, L24302, doi:10.1029/2011GL049762.
- Brocher, T. M. (2005), Empirical relations between elastic wave speeds and density in the Earth's crust, *Bull. Seismol. Soc. Am.*, **95**, 2081–2092.
- Bürgmann, R., M. G. Kogan, G. M. Steblow, G. Hilley, V. E. Levin, and E. Apel (2005), Interseismic coupling and asperity distribution along the Kamchatka subduction zone, *J. Geophys. Res.*, **110**, B07405, doi:10.1029/2005JB003648.
- Bürgmann, R., G. Hilley, A. Ferretti, and F. Novali (2006), Resolving vertical tectonics in the San Francisco Bay Area from permanent scatterer InSAR and GPS analysis, *Geology*, **34**(3), 221–224, doi:10.1130/G22064.1.
- Chen, G., X. Xu, X. Wen, and G. Yu (2008), Kinematic transformation and slip partitioning of northern to eastern active boundary belt of Sichuan-Yunnan block [in Chinese with English abstract], *Seismol. Geol.*, **30**(1), 58–85.
- Clark, M. K., and L. H. Royden (2000), Topographic ooze: Building the eastern margin of Tibet by lower crustal flow, *Geology*, **28**, 703–706.
- Clark, M. K., J. W. M. Bush, and L. H. Royden (2005), Dynamic topography produced by lower crustal flow against rheological strength heterogeneities bordering the Tibetan Plateau, *Geophys. J. Int.*, **162**, 575–590.
- Comninou, M., and J. Dundurs (1975), The angular dislocation in a half space, *J. Elasticity*, **5**, 203–216.
- Copley, A. (2008), Kinematics and dynamics of the southeastern margin of the Tibetan Plateau, *Geophys. J. Int.*, **174**, 1081–1100.
- Copley, A., and D. McKenzie (2007), Models of crustal flow in the India-Asia collision zone, *Geophys. J. Int.*, **169**, 683–698.
- Deng, Q., Y. Chang, K. Hsu, and F. Fan (1979), On the tectonic stress field in China and its relation to plate movement, *Phys. Earth Planet. Inter.*, **18**, 257–273.
- Deng, Q., P. Zhang, Y. Ran, X. Yang, W. Min, and Q. Chu (2003), Basic characteristics of active tectonics of China, *Sci. China, Ser. D Earth Sci.*, **46**, 356–372.
- Desbrun, M., M. Meyer, P. Schroder, and A. H. Barr (1999), Implicit fairing of irregular meshes using diffusion and curvature flow, *SIGGRAPH*, **99**, 317–324.
- Dragert, H., K. Wang, and T. S. James (2001), A silent slip event on the deeper Cascadia subduction interface, *Science*, **292**(5521), 1525–1528.
- Elliott, J. R., J. Biggs, B. Parsons, and T. J. Wright (2008), InSAR slip rate determination on the Altyn Tagh fault, northern Tibet, in the presence of topographically correlated atmospheric delays, *Geophys. Res. Lett.*, **35**, L12309, doi:10.1029/2008GL033659.
- Evans, E. L., J. P. Loveless, and B. J. Meade (2012), Geodetic constraints on San Francisco Bay Area fault slip rates and potential seismogenic asperities on the partially creeping Hayward fault, *J. Geophys. Res.*, **117**, B03410, doi:10.1029/2011JB008398.
- Fu, Y. V., A. Li, and Y. J. Chen (2010), Crustal and upper mantle structure of southeast Tibet from Rayleigh wave tomography, *J. Geophys. Res.*, **115**, B12323, doi:10.1029/2009JB007160.
- Fukahata, Y., and M. Matsuzura (2005), General expressions for internal deformation fields due to a dislocation source in a multilayered elastic halfspace, *Geophys. J. Int.*, **161**, 507–521.
- Fukahata, Y., and M. Matsuzura (2006), Quasi-static internal deformation due to a dislocation source in a multilayered elastic-viscoelastic half-space and an equivalence theorem, *Geophys. J. Int.*, **166**, 418–434.
- Fukahata, Y., A. Nishitani, and M. Matsuzura (2004), Geodetic data inversion using ABIC to estimate slip history during one earthquake cycle with viscoelastic slip-response functions, *Geophys. J. Int.*, **161**, 507–521.
- He, H., and J. Ren (2003), Holocene earthquakes on the Zemuhe fault in southwestern China, *Ann. Geophys.*, **46**(5), 1035–1051.
- Heidbach, O., and Z. Ben-Avraham (2007), Stress evolution and seismic hazard of the Dead Sea fault system, *Earth Planet. Sci. Lett.*, **257**, 299–312.
- Hu, J., X. Xu, H. Yang, L. Wen, and G. Li (2011), S receiver function analysis of the crustal and lithospheric structures beneath eastern Tibet, *Earth Planet. Sci. Lett.*, **306**, 77–85.
- Hyodo, M., and K. Hirahara (2003), A viscoelastic model of interseismic strain concentration in Niigata-Kobe tectonic zone of central Japan, *Earth Planets Space*, **55**, 667–675.
- Jiang, G., C. Xu, Y. Wen, Y. Liu, Z. Yin, and J. Wang (2013), Inversion for coseismic slip distribution of the 2010  $M_w$ 6.9 Yushu earthquake from InSAR data using angular dislocations, *Geophys. J. Int.*, **194**(2), 1011–1022.
- Jiang, G., C. Xu, Y. Wen, X. Xu, K. Ding, and J. Wang (2014), Contemporary tectonic stressing rates of major strike-slip faults in the Tibetan Plateau from GPS observations using least squares collocation, *Tectonophysics*, **615–616**, 85–95.
- Johnson, K. M., and J. Fukuda (2010), New methods for estimating the spatial distribution of locked asperities and stress-driven interseismic creep on faults with application to the San Francisco Bay Area, California, *J. Geophys. Res.*, **115**, B12408, doi:10.1029/2010JB007703.
- Johnson, K. M., and P. Segall (2004), Viscoelastic earthquake cycle models with deep stress-driven creep along the San Andreas fault system, *J. Geophys. Res.*, **109**, B10403, doi:10.1029/2004JB003096.
- Jónsson, S., H. Zebker, P. Segall, and F. Amelung (2002), Fault slip distribution of the 1999  $M_w$ 7.1 Hector Mine, California, earthquake, estimated from satellite radar and GPS measurements, *Bull. Seismol. Soc. Am.*, **92**, 1377–1389.

- Kanda, R. V. S., E. A. Hetland, and M. Simons (2013), An asperity model for fault creep and interseismic deformation in northeastern Japan, *Geophys. J. Int.*, 192(1), 38–57, doi:10.1093/gji/ggs028.
- Kato, N., X. Lei, and X. Wen (2007), A synthetic seismicity model for the Xianshuhe fault, southwestern China: Simulation using a rate- and state-dependent friction law, *Geophys. J. Int.*, 169, 286–300.
- Li, H., W. Su, C.-Y. Wang, and Z. Huang (2009), Ambient noise Rayleigh wave tomography in western Sichuan and eastern Tibet, *Earth Planet. Sci. Lett.*, 282, 201–211.
- Li, H., S. Li, X.-D. Song, M. Gong, X. Li, and J. Jia (2012), Crustal and uppermost mantle velocity structure beneath northwestern China from seismic ambient noise tomography, *Geophys. J. Int.*, 188, 131–143.
- Liang, S., W. Gan, C. Shen, G. Xiao, J. Liu, W. Chen, X. Ding, and D. Zhou (2013), Three-dimensional velocity field of present-day crustal motion of the Tibetan Plateau derived from GPS measurements, *J. Geophys. Res. Solid Earth*, 118, 5722–5732, doi:10.1002/2013JB010503.
- Liu, Y. (2014), Source scaling relations and along-strike segmentation of slow slip events in a 3-D subduction fault model, *J. Geophys. Res. Solid Earth*, 119, 6512–6533, doi:10.1002/2014JB011144.
- Liu, Q.-Y., Y. Li, J.-H. Chen, B. Guo, S.-C. Li, J. Wang, X.-Q. Zhang, and S.-H. Qi (2009), Wenchuan  $M_3$ .8.0 earthquake: Preliminary study of the  $S$  wave velocity structure of the crust and upper mantle [in Chinese with English abstract], *Chin. J. Geophys.*, 52(2), 309–319.
- Ludwig, W. J., J. E. Nafe, and C. L. Drake (1970), Seismic refraction, in *The Sea*, vol. 4, edited by A. E. Maxwell, pp. 53–84, Wiley-Interscience, New York.
- Maerten, F., P. Resor, D. Pollard, and L. Maerten (2005), Inverting for slip on three-dimensional fault surfaces using angular dislocations, *Bull. Seismol. Soc. Am.*, 95, 1654–1665.
- Matsu'ura, M., and T. Sato (1989), A dislocation model for the earthquake cycle at convergent plate boundaries, *Geophys. J. Int.*, 96, 23–32.
- Matsu'ura, M., D. D. Jackson, and A. Cheng (1986), Dislocation model for aseismic crustal deformation at Hollister, California, *J. Geophys. Res.*, 91(B12), 12,661–12,674, doi:10.1029/JB091iB12p12661.
- McCaffrey, R. (2005), Block kinematics of the Pacific-North America plate boundary in the southwestern United States from inversion of GPS, seismological, and geologic data, *J. Geophys. Res.*, 110, B07401, doi:10.1029/2004JB003307.
- McCaffrey, R., L. M. Wallace, and J. Beavan (2008), Slow slip and frictional transition at low temperature at the Hikurangi subduction zone, *Nat. Geosci.*, 1, 316–320.
- Meade, B. J., and J. P. Loveless (2009), Block modeling with connected fault network geometries and a linear elastic coupling estimator in spherical coordinates, *Bull. Seismol. Soc. Am.*, 99(6), 3124–3139.
- Noda, H., and N. Lapusta (2013), Stable creeping fault segments can become destructive as a result of dynamic weakening, *Nature*, 492, 518–521.
- Nur, A., and G. Mavko (1974), Postseismic viscoelastic rebound, *Science*, 183(4121), 204–206, doi:10.1126/science.183.4121.204.
- Ohta, Y., J. T. Freymueller, S. Hreinsdóttir, and H. Suito (2006), A large slow slip event and the depth of the seismogenic zone in the south central Alaska subduction zone, *Earth Planet. Sci. Lett.*, 247, 108–116.
- Papadimitriou, E., X. Wen, V. Karakostas, and X. Jin (2004), Earthquake triggering along the Xianshuhe fault zone of western Sichuan, China, *Pure Appl. Geophys.*, 161, 1683–1707.
- Peyret, M., F. Masson, H. Yavasoglu, S. Ergintav, and R. Reilinger (2013), Present-day strain distribution across a segment of the central bend of the North Anatolian fault zone from a persistent scatterer InSAR analysis of the ERS and Envisat archives, *Geophys. J. Int.*, 192, 929–945.
- Pollitz, F. F., P. McCrory, J. Svart, and J. Murray (2008), Dislocation models of interseismic deformation in the western United States, *J. Geophys. Res.*, 113, B04413, doi:10.1029/2007JB005174.
- Qian, H., X. Wu, S. Ma, C. Cai, and H. Tian (1990), Prehistorical earthquakes on the north segment of the Anninghe fault and their significance to seismological research [in Chinese with English abstract], *Earthquake Res. China*, 6(4), 43–49.
- Ran, H. L., and H. L. He (2006), Research on the magnitude and recurrence interval of characterized earthquakes with  $M \geq 6.7$  along the northwestern portion of the Xianshuhe fault zone in western Sichuan, China [in Chinese with English abstract], *Chin. J. Geophys. Res.*, 49(1), 153–161.
- Ran, Y., L. Chen, J. Cheng, and H. Gong (2008), Late Quaternary surface deformation and rupture behavior of strong earthquake on the segment north of Mianning of the Anninghe fault, *Sci. China, Ser. D Earth Sci.*, 51, 1224–1237.
- Ren, J.-W., and P. Li (1989), Earthquake-caused landforms and paleoseismic study on the northern segment of the Zemuhe fault [in Chinese with English abstract], *Seismol. Geol.*, 11(1), 27–34.
- Royden, L. H., B. C. Burchfiel, and R. D. van der Hilst (2008), The geological evolution of the Tibetan Plateau, *Science*, 321, 1054–1058, doi:10.1126/science.1155371.
- Savage, J., and R. Burford (1973), Geodetic determination of relative plate motion in central California, *J. Geophys. Res.*, 78, 832–845, doi:10.1029/JB078i005p00832.
- Savage, J., and W. H. Prescott (1978), Asthenosphere readjustment and the earthquake cycle, *J. Geophys. Res.*, 83(B7), 3369–3376, doi:10.1029/JB083iB07p03369.
- Savage, J. C., and R. O. Burford (1970), Accumulation of tectonic strain in California, *Bull. Seismol. Soc. Am.*, 60, 1877–1896.
- Savage, J. C., and M. Lisowski (1998), Viscoelastic coupling model of the San Andreas fault along the big bend, southern California, *J. Geophys. Res.*, 103(B4), 7281–7292, doi:10.1029/98JB00148.
- Savage, J. C., W. Gan, and J. L. Svart (2001), Strain accumulation and rotation in the eastern California shear zone, *J. Geophys. Res.*, 106(B10), 21,995–22,007, doi:10.1029/2000JB000127.
- Schmidt, D. A., R. Bürgmann, R. M. Nadeau, and M. d'Alessio (2005), Distribution of aseismic slip rate on the Hayward fault inferred from seismic and geodetic data, *J. Geophys. Res.*, 110, B08406, doi:10.1029/2004JB003397.
- Schwartz, D. P., and K. J. Coppersmith (1984), Fault behavior and characteristic earthquakes: Examples from the Wasatch and San Andreas fault zones, *J. Geophys. Res.*, 89(B7), 5681–5698, doi:10.1029/JB089iB07p05681.
- Shen, Z.-K., J. Lu, M. Wang, and R. Bürgmann (2005), Contemporary crustal deformation around the southeast borderland of the Tibetan Plateau, *J. Geophys. Res.*, 110, B11409, doi:10.1029/2004JB003421.
- Stark, P. B., and R. L. Parker (1995), Bounded variable least squares: An algorithm and application, *J. Comput. Stat.*, 10, 129–141.
- Sun, X., X. Bao, M. Xu, D. W. Eaton, X. Song, L. Wang, Z. Ding, N. Mi, D. Yu, and H. Li (2014), Crustal structure beneath SE Tibet from joint analysis of receiver functions and Rayleigh wave dispersion, *Geophys. Res. Lett.*, 41, 1479–1484, doi:10.1002/2014GL059269.
- Tapponier, P., and P. Molnar (1977), Active faulting and tectonics in China, *J. Geophys. Res.*, 82, 2905–2930, doi:10.1029/JB082i020p02905.
- Tian, Q.-J., Z.-K. Ren, and J.-L. Zhang (2008), Study of paleoearthquakes by combined trench on Zemuhe fault around Daqingliangzi, Xichang, Sichuan [in Chinese with English abstract], *Seismol. Geol.*, 30(2), 400–411.
- Wang, C. Y., W. B. Han, J. P. Wu, H. Lou, and W. W. Chan (2007), Crustal structure beneath the eastern margin of the Tibetan Plateau and its tectonic implications, *J. Geophys. Res.*, 112, B07307, doi:10.1029/2005JB003873.

- Wang, C. Y., H. Lou, P. G. Silver, L. Zhu, and L. Chang (2010), Crustal structure variation along 30°N in the eastern Tibetan Plateau and its tectonic implications, *Earth Planet. Sci. Lett.*, 289, 367–376.
- Wang, H., T. J. Wright, and J. Biggs (2009), Interseismic slip rate of the northwestern Xianshuihe fault from InSAR data, *Geophys. Res. Lett.*, 36, L03302, doi:10.1029/2008GL036560.
- Wang, H., Y. Ran, Y. Li, F. Gomez, and L. Chen (2013), Holocene palaeoseismologic record of the earthquakes on the Zemuhe fault on the southeastern margin of the Tibetan Plateau, *Geophys. J. Int.*, 193(1), 11–28.
- Wang, K., J. He, H. Dragert, and T. S. James (2001), Three-dimensional viscoelastic interseismic deformation model for the Cascadia subduction zone, *Earth Planet. Space*, 53, 295–306.
- Wang, K., Y. Hu, and J. He (2012), Deformation cycles of subduction earthquakes in a viscoelastic Earth, *Nature*, 484, 327–332.
- Wang, W., J. Wu, L. Fang, G. Lai, T. Yang, and Y. Cai (2014), S wave velocity structure in southwest China from surface wave tomography and receiver functions, *J. Geophys. Res. Solid Earth*, 119, 1061–1078, doi:10.1002/2013JB010317.
- Wang, Y., W. W. Chan, and W. D. Mooney (2003), Three-dimensional velocity structure of crust and upper mantle in southwestern China and its tectonic implications, *J. Geophys. Res.*, 108(B9), 2442, doi:10.1029/2002JB001973.
- Wang, Y., W. D. Mooney, X. Yuan, and N. Okaya (2013), Crustal structure of the northeastern Tibetan Plateau from the southern Tarim basin to the Sichuan basin, China, *Tectonophysics*, 584, 191–208.
- Welstead, S. T. (1999), *Fractal and Wavelet Image Compression Techniques*, pp. 51–54, SPIE Optical Engineering Press, Bellingham, Wash.
- Wen, X. (2000), Character of rupture segmentation of the Xianshuihe-Anninghe-Zemuhe fault zone, western Sichuan [in Chinese with English abstract], *Seismol. Geol.*, 22(3), 239–249.
- Wen, X.-Z., S.-L. Ma, X.-W. Xu, and Y.-N. He (2008a), Historical pattern and behavior of earthquake ruptures along the eastern boundary of the Sichuan-Yunnan faulted block, southwestern China, *Phys. Earth Planet. Inter.*, 168, 16–36.
- Wen, X.-Z., J. Fan, G.-X. Yi, Y.-W. Deng, and F. Long (2008b), A seismic gap on the Anninghe fault in western Sichuan, China, *Sci. China, Ser. D Earth Sci.*, 51(10), 1375–1387.
- Xu, X., X. Wen, R. Zheng, W. Ma, F. Song, and G. Yu (2003), Pattern of latest tectonic motion and dynamics of faulted blocks in Yunnan and Sichuan, *Sci. China, Ser. D Earth Sci.*, 33(Suppl.), 151–162.
- Xu, X., X. Wen, G. Chen, and G. Yu (2008), Discovery of the Longriba fault zone in eastern Bayan Har block, China, and its tectonic implication, *Sci. China, Ser. D Earth Sci.*, 51, 1209–1223.
- Xu, X., Z. Ding, D. Shi, and X. Li (2013), Receiver function analysis of crustal structure beneath the eastern Tibetan Plateau, *J. Asian Earth Sci.*, 73, 121–127.
- Xu, Z.-J., and X. Song (2010), Joint inversion for crustal and Pn velocities and Moho depth in eastern margin of the Tibetan Plateau, *Tectonophysics*, 491, 185–193.
- Yang, Y., M. H. Ritzwoller, Y. Zheng, W. Shen, A. L. Levshin, and Z. Xie (2012), A synoptic view of the distribution and connectivity of the midcrustal low-velocity zone beneath Tibet, *J. Geophys. Res.*, 117, B04303, doi:10.1029/2011JB008810.
- Yang, Z., F. Wang, Y. Duan, C. Zhang, J. Zhao, J. Zhang, and B. Liu (2011), Basement structure of southeastern boundary region of Sichuan-Yunnan active blocks: Analysis result of Yanyuan-Xichang-Zhaojue-Mahu deep seismic sounding profile [in Chinese with English abstract], *Acta Seismol. Sin.*, 33(4), 431–442.
- Yao, H., C. Beghein, and R. D. van der Hilst (2008), Surface wave array tomography in SE Tibet from ambient seismic noise and two-station analysis: II. Crustal and upper mantle structure, *Geophys. J. Int.*, 173, 205–219.
- Yi, G., X. Wen, J. Fan, and S. Wang (2004), Assessing current faulting behaviors and seismic risk of the Anninghe-Zemuhe fault zone from seismicity parameters [in Chinese with English abstract], *Acta Seismol. Sin.*, 26(3), 294–303.
- Yi, G.-X., J. Fang, and X.-Z. Wen (2005), Study on faulting behavior and fault segments for potential strong earthquake risk along the central southern segment of Xianshuihe fault zone based on current seismicity [in Chinese with English abstract], *Earthquake*, 25(1), 58–66.
- Yi, G.-X., X.-Z. Wen, and Y.-J. Su (2008), Study on the potential strong-earthquake risk for the earthern boundary of the Sichuan-Yunnan active faulted block, China [in Chinese with English abstract], *Chin. J. Geophys.*, 51(6), 1719–1725.
- Zhang, P.-Z. (2013), A review on active tectonics and deep crustal processes of the western Sichuan region, eastern margin of the Tibetan Plateau, *Tectonophysics*, 584, 7–22.
- Zhang, Z., Y. Deng, J. Teng, C. Wang, R. Gao, Y. Chen, and W. Fan (2011), An overview of the crustal structure of the Tibetan Plateau after 35 years of deep seismic soundings, *J. Asian Earth Sci.*, 40, 977–989.
- Zhou, H., H.-L. Liu, and H. Kanamori (1983), Source processes of larger earthquakes along the Xianshuihe fault in southwestern China, *Bull. Seismol. Soc. Am.*, 73(2), 537–551.
- Zhou, L., J. Xie, W. Shen, Y. Zheng, Y. Yang, H. Shi, and M. H. Ritzwoller (2012), The structure of the crust and uppermost mantle beneath south China from ambient noise and earthquake tomography, *Geophys. J. Int.*, 189, 1565–1583.
- Zhou, R., Y. He, T. Yang, Q. He, and X. Li (2001a), Slip rate and strong earthquake rupture on the Moxi-Mianning segment along the Xianshuihe-Anninghe fault zone [in Chinese with English abstract], *Earthquake Res. China*, 17(3), 253–262.
- Zhou, R., Y. He, Z. Huang, X. Li, and T. Yang (2001b), The slip rate and strong earthquake recurrence interval on the Qianning-Kangding segment of the Xianshuihe fault zone [in Chinese with English abstract], *Acta Seismol. Sin.*, 23(3), 263–273.
- Zhu, A.-L., X.-W. Xu, Y.-S. Zhou, J.-Y. Yin, W.-J. Gan, and G.-H. Chen (2005), Relocation of small earthquakes in western Sichuan, China, and its implications for active tectonics [in Chinese with English abstract], *Chin. J. Geophys.*, 48(3), 629–636.